

## **AC DATA ANALYSIS OF SOLID ELECTROLYTES**

**Ian M. Hodge**  
**Department of Physics**  
**Rochester Institute of Technology**  
**Rochester, New York 14623**

### **ABSTRACT**

Mathematical techniques for analyzing the ac conductivity of solid electrolytes are reviewed, with emphasis being placed on solid electrolytes and intergranular and other interfacial effects. Methods for determining the limiting low frequency conductivity in the absence of a conductivity plateau are described and illustrated with specific examples from the literature. Formalisms for evaluating the electrical relaxation properties of bulk solid electrolytes, and determining the average resistive and capacitive components of intergranular and other interfacial impedances, are described. A novel method for analyzing the dielectric Maxwell-Wagner effect is described. Elementary complex number algebra and its application to ac circuits, and dielectric and conductivity relaxation phenomenology, are presented.

## PROLOGUE

This paper was written many years ago as a summary of what this author knew at the time about the mathematical analysis of impedance spectroscopic data on solid electrolytes. For a variety of reasons it was not published then, but inquiries and comments received since it was circulated around the solid electrolyte community led me to believe that the paper was much more useful to workers in the field than I had imagined. It seemed appropriate to publish it at this time because of the continuing scientific interest in the area, and because the computer interfaced impedance analyzers that have become commonplace generate a lot of raw data that is in a convenient form for further mathematical analysis. Because of the paper's history, the references to illustrative experimental data are not recent. However, since it is the mathematical tools that are reviewed, and not experimental data *per se*, and because these mathematical techniques have not changed with time, it was not considered important to update the examples.

Some minor errors in the original manuscript have been corrected and the clarity of presentation has also been improved.

## 1. INTRODUCTION

Solid electrolytes have been a continuing subject of research ever since the discovery of the extraordinarily high ionic conductivity of sodium beta alumina in 1967 [1]. This interest has in large part been driven by applications to high energy density batteries. There has been a parallel development of mathematical formalisms for the analysis of ac data, that are assuming increasing importance as automated impedance analyzers become more common. Applications of these formalisms to solid electrolytes are the subject of this review.

The large electrical conductivity of solid electrolytes demands a mathematical description that differs from that used in dielectric relaxation. The distinction is important, because the use of an inappropriate formalism can in many cases result in a substantial loss of information. For example, the limiting low frequency conductivity can often only be determined, in the absence of a conductivity plateau, if an appropriate impedance function such as the complex resistivity or electric modulus is used. Formalisms that are suited to conductivity analysis are also useful for analyzing interfacial effects in dielectric media, such as the Maxwell-Wagner effect. The analysis of interfacial polarization phenomena provides a good illustration of the importance of using the correct formalisms to extract the maximum amount of information from experimental data, and this is explored at length using specific applications to literature data.

The review is divided into five sections. Following this introduction, the second section summarizes elementary complex variable algebra and its application to simple ac circuits. The third section treats dielectric relaxation from a phenomenological viewpoint, and relates it to the circuit theory of the first section. Section Four extends the dielectric phenomenology to conductivity relaxation in solid electrolytes, and introduces the formalisms that are particularly suited to its analysis. Section Five is devoted to the illustration of these formalisms using experimental data from the literature, although no attempt is made to review experimental data *per se*. The properties of frequently used distribution functions are summarized in an Appendix, and empirical equations for extracting distribution function parameters from loss spectra are included.

Several topics are excluded for the sake of brevity and a sharp focus. The large field of electrode kinetics is omitted - it is assumed that the applied potential is below the decomposition potential of the electrode-electrolyte combination being studied, so that Faradaic impedances can be neglected. Thus blocking electrodes will usually be assumed, although a few exceptions are made to illustrate specific points.

The SI system of units is used throughout.

## 2. COMPLEX NUMBERS and AC CIRCUITS

### 2.1 Complex Numbers.

A complex number,  $z$ , is a number pair whose components are termed the real,  $x$ , and imaginary,  $y$ , parts. It is expressed as

$$z = x + iy, \quad (1)$$

where  $i = (-1)^{1/2}$ . Thus, for example,

$$z^2 = (x^2 + y^2) + i(2xy). \quad (2)$$

A function that is central to the application of complex numbers to relaxation phenomena is the exponential function,

$$\exp(z) = \exp(x + i \cdot y) = \exp(x) \cdot \exp(i \cdot y) = \exp(x) \cdot [\cos(y) + i \cdot \sin(y)]. \quad (3)$$

The cosine function of the real variable,  $y$ , can therefore be written as

$$\cos(y) = \text{Re}[\exp(iy)] \quad (4)$$

and the sine function as

$$\sin(y) = \text{Re}[-i \cdot \exp(iy)], \quad (5)$$

where  $\text{Re}$  denotes the real component of a complex function. Since the sine and cosine functions differ only by the phase angle  $\pi/2$ , eqs (4) and (5) demonstrate that  $i$  shifts the phase angle by  $\pi/2$ . The usefulness of complex numbers in describing physical properties that are measured with sinusoidally varying excitations derives from this property of  $i$ .

## 2.2 Analytical Functions of a Complex Variable.

Of all the possible functions of a complex variable, only one kind is generally useful for describing physical properties. These are the analytical functions, defined as being single valued and uniquely differentiable, the latter meaning that differentiation with respect to  $z$  does not depend on the direction of differentiation in the complex plane (for an excellent account of the applications of complex numbers, see reference [3]). Thus, differentiation parallel to the  $x$  axis ( $\partial/\partial x$ ) produces the same result as differentiation parallel to the  $y$  axis ( $\partial/\partial y$ ), and this results in the real and imaginary parts of an analytical function being related to one another. For example, the Cauchy-Riemann conditions (included here for the sake of completeness), for an analytical function  $f(z)$  expressed as

$$f(z) = f(x + i \cdot y) = u(x, y) + i \cdot v(x, y) \quad (6)$$

are

$$\left(\frac{\partial u}{\partial x}\right) = \left(\frac{\partial v}{\partial y}\right), \quad (7)$$

$$\left(\frac{\partial u}{\partial y}\right) = -\left(\frac{\partial v}{\partial x}\right). \quad (8)$$

The exponential function conforms to the Cauchy-Riemann conditions, for example, and is therefore analytical. Equations (7) and (8) reveal that  $u$  and  $v$  are harmonic functions, because they obey the two dimensional Laplace equations

$$\nabla^2 u = \nabla^2 v = 0 \quad (9)$$

Another condition that must be met for a function to be analytical is that it be single-valued. There are also other conditions that are necessary for mathematical consistency but which need not concern us here [3]. Integral versions of the Cauchy-Riemann conditions are known as the Hilbert relations (derived from the Cauchy theorem that also need not concern us here):

$$u(z) = \frac{1}{\pi} \int_{-\infty}^{+\infty} \frac{v(\omega) \cdot d\omega}{(\omega - z)}, \quad (10)$$

$$v(z) = -\frac{1}{\pi} \int_{-\infty}^{+\infty} \frac{u(\omega) \cdot d\omega}{(\omega - z)}. \quad (11)$$

These, together with the crossing relations (12) below, give the Kronig-Kramers dispersion formulae. The crossing relations are

$$\begin{aligned}
u(x) &= u(-x) \\
\text{and} & \\
v(x) &= -v(-x)
\end{aligned} \tag{12}$$

where  $x$  is real. Insertion of these relations into the Hilbert relations, in order to eliminate integration over a negative real argument (e.g. frequency) gives the Kronig-Kramers relationships

$$u(x) = \frac{2}{\pi} \int_{-\infty}^{+\infty} \frac{\omega \cdot v(\omega) \cdot d\omega}{(\omega^2 - x^2)} \tag{13}$$

$$v(x) = \frac{2 \cdot x}{\pi} \int_{-\infty}^{+\infty} \frac{u(\omega) \cdot d\omega}{(x^2 - \omega^2)} \tag{14}$$

### 2.3 Elementary AC Circuits

Sinusoidally varying voltages and currents are fundamental to impedance spectroscopy, making complex numbers and the exponential function especially useful for describing them. Consider for example a sinusoidally varying voltage  $V = V_0 \cos(\omega \cdot t)$  that is applied across a resistance,  $R_p$ , in parallel with a capacitance,  $C_p$ . The current through the resistance,  $I_R$ , is given by

$$I_R = \frac{V}{R_p} = \frac{V_0 \cdot \cos(\omega \cdot t)}{R_p} = V_0 \cdot \cos(\omega \cdot t) \cdot G_p = \text{Re}[V_0 \cdot G_p \cdot \exp(i \cdot \omega \cdot t)], \tag{15}$$

where  $G_p$  is the conductance. The current through the capacitance,  $I_C$ , is given by

$$I_C = \frac{dq_C}{dt} = C_p \cdot \frac{dV}{dt} = -V_0 \cdot \omega \cdot C_p \cdot \sin(\omega \cdot t) = \text{Re}[i \cdot V_0 \cdot \omega \cdot C_p \exp(i \cdot \omega \cdot t)] \tag{16}$$

where  $q_C$  is the charge on the capacitor. Thus the total current is

$$\begin{aligned}
I &= I_R + I_C = V_0 \cdot G_p \cdot \cos(\omega \cdot t) - V_0 \cdot \omega \cdot C_p \cdot \sin(\omega \cdot t) \\
&= \text{Re}\left\{ [G_p + i \cdot \omega \cdot C_p] \cdot V_0 \cdot \exp(i \cdot \omega \cdot t) \right\}
\end{aligned} \tag{17}$$

The phase relations for the current can therefore be succinctly expressed by defining the parallel resistance and capacitance either as a complex admittance,  $A^*$ , given by

$$A^* = (G_p + i \cdot \omega \cdot C_p) \tag{18}$$

Similarly, the effective ac resistance, or complex impedance  $Z^*$ , is given by

$$\begin{aligned} Z^* &= \frac{1}{A^*} = \frac{1}{(G_p + i \cdot \omega \cdot C_p)} \\ &= \frac{G_p}{(G_p^2 + \omega^2 \cdot C_p^2)} - \frac{i \cdot \omega \cdot C_p}{(G_p^2 + \omega^2 \cdot C_p^2)} \end{aligned} \quad (19)$$

Equation (19) can be rewritten as

$$Z^* = \frac{R_p}{(1 + \omega^2 \cdot \tau_\sigma^2)} - \frac{i \cdot R_p \cdot \omega \cdot \tau_\sigma}{(1 + \omega^2 \cdot \tau_\sigma^2)}, \quad (20)$$

where

$$\tau_E = R_p \cdot C_p \quad (21)$$

is the Maxwell relaxation time [4]. The reason for the subscript  $E$  is given below. When normalized by the cell constant,  $k$  (dimensions  $\text{m}^{-1}$  from the effective electrode spacing divided by the effective electrode area), the quantities  $A^*$  and  $Z^*$  become the complex conductivity,  $\sigma^* = k \cdot A^*$ , and complex resistivity,  $\rho^* = Z^*/k$ .

The complex capacitance is given by

$$C^* = \frac{A^*}{i \cdot \omega} = C_p - \frac{i \cdot G_p}{\omega} \quad (22)$$

### 3 FUNDAMENTALS OF DIELECTRIC RELAXATION

#### 3.1 General Concepts and Basic Formalisms

A freely rotating dipole in a sinusoidally varying electric field, whose angular frequency is sufficiently low that the dipole can keep up with the field, behaves as a pure capacitance,  $C_p$ . The current lags behind the field by  $\pi/2$  radians (eqs. 10), and the complex admittance is given by

$$A^* = i \cdot \omega \cdot C_p \quad (23)$$

If the dipole cannot keep up with the field because of friction with the environment, it will lag by an additional angle  $\delta$  and a component of the current appears in phase with the voltage. Thus eq. (16) is replaced by

$$\begin{aligned}
I_c &= -V_0 \cdot \omega \cdot C_p \cdot \sin(\omega \cdot t - \delta) \\
&= -V_0 \cdot \omega \cdot C_p \cdot [\cos(\omega \cdot t) \cdot \sin(\delta) - \sin(\omega \cdot t) \cdot \cos(\delta)] \\
&= \text{Re}\{i \cdot V_0 \cdot \omega \cdot C_p [\cos(\delta) - i \cdot \sin(\delta)] \cdot \exp(i \cdot \omega \cdot t)\}
\end{aligned} \tag{24}$$

Comparing eq. (24) with eqs. (17) and (18) reveals that

$$A^* = \omega \cdot C_p \cdot \sin(\delta) + i \cdot \omega \cdot C_p \cdot \cos(\delta) \tag{25}$$

so that

$$C^* = C_p \cdot \cos(\delta) - i \cdot C_p \cdot \sin(\delta) = C' - i \cdot C'' \tag{26}$$

Equation (22) then implies

$$G_p(\text{effective}) = \omega \cdot C_p \cdot \sin(\delta) \tag{27}$$

and

$$C_p(\text{effective}) = C_p \cdot \cos(\delta) \tag{28}$$

Note that at low frequencies, when the lag angle tends to zero, the effective capacitance equals  $C_p$ , as must be. When normalized by the geometric capacitance,  $C_0 = \frac{\epsilon_0}{k}$ , associated with the cell constant  $k$  where  $\epsilon_0$  is the vacuum permittivity ( $8.854 \times 10^{-12}$ )  $\text{F m}^{-1}$ , the complex capacitance becomes the complex permittivity,  $\epsilon^* = \frac{C^*}{C_0}$ , so that

$$\epsilon^* = \epsilon' - i \cdot \epsilon'' \tag{29}$$

where

$$\epsilon' = \frac{C_p}{C_0} = \cos(\delta), \tag{30}$$

$$\epsilon'' = \frac{G_p}{\omega \cdot C_0} = \frac{\sigma}{\epsilon_0 \cdot \omega} = \sin(\delta) \tag{31}$$

and

$$\tan(\delta) = \frac{\varepsilon''}{\varepsilon'} = \frac{G_p}{\omega \cdot C_p}. \quad (32)$$

Note that  $\tan(\delta)$  is independent of the geometric capacitance  $C_0$ . Equations (25) and (29) - (31) imply that

$$A^* = i \cdot \omega \cdot C_0 \cdot \varepsilon^* \quad (33)$$

so that

$$\sigma^* = k \cdot A^* = i \cdot \omega \cdot \varepsilon_0 \cdot \varepsilon^* \quad (34)$$

and

$$\rho^* = \frac{1}{\sigma^*} = \frac{1}{k \cdot A^*} = \frac{1}{i \cdot \omega \cdot \varepsilon_0 \cdot \varepsilon^*}. \quad (35)$$

The complex electric modulus,  $M^*$ , is defined as the reciprocal of  $\varepsilon^*$ :

$$M^* \equiv \frac{1}{\varepsilon^*}. \quad (36)$$

Thus

$$M^* = i \cdot \omega \cdot C_0 \cdot Z^* = i \cdot \omega \cdot \varepsilon_0 \cdot \rho^* \quad (37)$$

The dielectric loss  $\varepsilon''$  is related to the optical absorption coefficient  $\alpha$  (neper  $\text{m}^{-1}$ ) by

$$\varepsilon''(\omega) = \frac{n'(\omega) \cdot \alpha(\omega) \cdot c}{\omega} \quad (38)$$

where  $n'$  is the real component of the complex refractive index and  $c$  is the speed of light in vacuo ( $3.00 \times 10^8$  m/s).

The functions  $\sigma^*$ ,  $\varepsilon^*$ ,  $\rho^*$  and  $M^*$  are all analytical functions, whose components conform to the Cauchy-Riemann and Kronig-Kramers equations.

### 3.2 Relaxation Times

Dielectric relaxation can also be determined in the time domain. If an electric field across a dielectric sample is instantaneously increased from zero to  $E_0$  and kept constant thereafter, the initially randomized dipoles will orient themselves over time and the polarization,  $P$ , and displacement,  $D$ , will decrease (recall that  $D = \epsilon_0 \cdot E + P$ ):

$$P_E(t) = P_E(t) \cdot [1 - \phi_E(t)] \Rightarrow D_E(t) = D_E(t) \cdot [1 - \phi_E(t)] \quad (39)$$

where  $\phi_E(t)$  is the dielectric retardation function at constant  $E$ . The complex relative permittivity  $\epsilon^*(\omega)$  is related to the derivative of  $\epsilon(t) = D(t)/E_0$  by

$$\epsilon^* - \epsilon_\infty = (\epsilon_0 - \epsilon_\infty) \cdot \int_0^\infty -\left(\frac{d\phi_E}{dt}\right) \cdot \exp(-i \cdot \omega \cdot t) \cdot dt \quad (40)$$

where  $\epsilon_0$  and  $\epsilon_\infty$  (both real [5]) are the limiting low and high frequency limits of  $\epsilon'$ , respectively. In the simplest case,  $\phi_E(t)$  is exponential:

$$\phi_E(t) = \exp\left(-\frac{t}{\tau_E}\right), \quad (41)$$

where  $\tau_E$  is the dielectric retardation time at constant  $E$  [different from the relaxation time  $\tau_E$  of eq. (21)]. Insertion of eq. (41) into eq. (40) yields the Debye equation [6]:

$$\epsilon^* - \epsilon_\infty = \frac{\epsilon_0 - \epsilon_\infty}{1 + i \cdot \omega \cdot \tau_E}, \quad (42)$$

from which

$$\epsilon' - \epsilon_\infty = \frac{\epsilon_0 - \epsilon_\infty}{1 + \omega^2 \cdot \tau_E^2}, \quad (43)$$

$$\epsilon'' = \frac{(\epsilon_0 - \epsilon_\infty) \cdot \omega \cdot \tau_E}{1 + \omega^2 \cdot \tau_E^2} = (\epsilon_0 - \epsilon_\infty) \cdot \operatorname{sech}\left[\ln(\omega \cdot \tau_E)\right], \quad (44)$$

$$\tan(\delta) \equiv \left(\frac{\epsilon''}{\epsilon'}\right) = \frac{(\epsilon_0 - \epsilon_\infty) \cdot \omega \cdot \tau_E}{\epsilon_0 \cdot [1 + (\epsilon_\infty/\epsilon_0) \cdot \omega^2 \cdot \tau_E^2]}, \quad (45)$$

and

$$\sigma' = \text{Re}(\sigma^*) = e_0 \cdot \omega \cdot \varepsilon'' = \frac{(\varepsilon_0 - \varepsilon_\infty) \cdot (e_0 / \tau_E) \cdot \omega^2 \cdot \tau_E^2}{\varepsilon_0 \cdot [1 + (\varepsilon_\infty / \varepsilon_0) \cdot \omega^2 \cdot \tau_E^2]} \quad (46)$$

Note that  $\tan(\delta)$  has the same frequency dependence as  $\varepsilon''$ , but with a retardation time of  $(\varepsilon_\infty / \varepsilon_0)^{1/2} \cdot \tau_E$  rather than  $\tau_E$ . Equation (46) indicates that the conductivity increases from zero at low frequencies, to a high frequency limit of

$$\sigma_\infty = (\varepsilon_0 - \varepsilon_\infty) \cdot (e_0 / \tau_E) \quad (47)$$

### 3.3 Distribution Functions

If the retardation function is nonexponential, dielectric relaxation can be described in terms of a distribution of retardation times,  $g(\ln \tau_E)$ , defined by the relation

$$\phi_E(t) = \int_0^\infty g(\tau_E) \cdot \exp\left(-\frac{t}{\tau_E}\right) \cdot d\tau_E = \int_{-\infty}^\infty g(\ln \tau_E) \cdot \exp\left(-\frac{t}{\tau_E}\right) \cdot d \ln \tau_E \quad (48)$$

Equation (42) then generalizes to

$$\varepsilon^* - \varepsilon_\infty = (\varepsilon_0 - \varepsilon_\infty) \cdot \int_0^\infty \frac{g(\tau_E)}{1 + i \cdot \omega \cdot \tau_E} \cdot d\tau_E = (\varepsilon_0 - \varepsilon_\infty) \cdot \int_{-\infty}^\infty \frac{g(\ln \tau_E)}{1 + i \cdot \omega \cdot \tau_E} \cdot d \ln \tau_E \quad (49)$$

The distribution function can be characterized by its moments, given by

$$\langle \tau_E^n \rangle = \int_0^\infty \tau_E^n \cdot g(\tau_E) \cdot d\tau_E = \int_{-\infty}^\infty \tau_E^n \cdot g(\ln \tau_E) \cdot d \ln \tau_E \quad (50)$$

for the  $n^{\text{th}}$  moment. The distribution function is normalized so that its zero<sup>th</sup> moment is unity. In terms of  $\phi(t)$  the  $n^{\text{th}}$  moments are

$$\langle \tau_E^n \rangle = \left( \frac{1}{\Gamma(\omega)} \right) \cdot \int_0^\infty t^{n-1} \cdot \phi(t) \cdot dt \quad (51)$$

and

$$\langle \tau_E^{-n} \rangle = (-1)^n \cdot \left[ \frac{d^n(\phi_E)}{dt^n} \right]_{t=0} \quad (52)$$

If a limiting low frequency conductivity  $\sigma_0$  is present, this must be subtracted from the measured conductivity before the dielectric loss is calculated from eq. (34). If this is not done, the decrease in  $\varepsilon''$  as  $\omega \rightarrow 0$  predicted by eq. (44) will not occur, but will be masked by the rapid rise from the conductivity contribution

$$\varepsilon''_{\sigma} = \frac{\sigma_0}{\varepsilon_0 \cdot \omega} \quad (53)$$

It has been argued that this subtraction is physically meaningful only if the conductivity is unrelated to the dielectric loss process (as in aqueous solutions, for example). If the dielectric loss peak correlates with  $\sigma_0$ , as occurs in alkali silicate glasses [7-13], the subtraction of  $\sigma_0$  can be regarded as artificial and other methods of data analysis are preferred (although this position is not universally accepted). This is the principle reason for not using the complex permittivity in analyzing highly conducting materials, and is the subject of section 4.

### 3.4 Hamon Approximation

Time and frequency domain data can be related by the approximate Hamon relation [14]

$$\varepsilon''(\omega) \approx \left[ (\varepsilon - \varepsilon') \cdot \left( -\frac{dt}{dt} \right) \cdot \left( \frac{5 \cdot t}{\pi} \right) \right]_{\omega t = \pi/5}, \quad (54)$$

derived from the approximation that the normalized current is

$$i = \left( \frac{d\phi}{dt} \right) \sim t^{-n} \quad (55)$$

No comparably simple relation exists between  $\varepsilon''(\omega)$  and  $\phi(t)$ . Williams, Watts, Dev and North [15] have shown that, for the decay function

$$\phi(t) = \exp \left[ - \left( \frac{t}{\tau_0} \right)^\beta \right] \quad (56)$$

the Hamon approximation is accurate within 1% for  $\log_{10}(\omega \cdot \tau_0) \geq 0$ , but fails for  $\log_{10}(\omega \cdot \tau_0) < 0$  and  $\beta \geq 0.2$ . For high frequencies, therefore, eq. (54) offers an acceptable approximation to the frequency domain Williams-Watts function, which cannot be expressed in terms of named (i.e. tabulated or subroutine) functions.

### 3.5 Equivalent Circuits

The electrical response corresponding to an exponential decay function, the Debye relation eq. (42), is simulated by the equivalent circuit shown in Figure 1, in which the conductance corresponds to the zero frequency conductivity. Detailed discussions of the use of equivalent circuits are given in the literature [16], and we restrict ourselves here to noting that if, for a particular range of frequencies, the equivalent circuit of an experimental sample resembles that shown in Figure 1, then a dielectric loss will be observed in that frequency range. Generally speaking, a resistance and capacitance in series is often sufficient to produce dielectric loss behavior. An example of such a series circuit is electrode polarization, which at low frequencies may be approximated by a capacitance in series with the low frequency resistance of the sample. In this case a dielectric loss is observed with a retardation time given by the product of the polarization capacitance and sample resistance. Electrode polarization effects in solid electrolytes can often be a serious problem, and are discussed further in section 4.3 below.

### 3.6 Dielectric Relaxation in the Temperature Domain

For many dielectric functions,  $\omega$  and  $\tau$  are interchangeable variables. Since  $\tau$  often varies strongly with temperature, temperature can be used as an experimental variable to replace frequency. This is often done for experimental simplicity, and because the changes in  $\tau$  with temperature cover a much wider range in frequency than that of most audio and sub-audio frequency generators and detectors. If the temperature dependence of  $\tau$  is approximated over small ranges in temperature  $T$  by the Arrhenius relation

$$\tau_E = \tau_0 \exp\left(\frac{E_A}{R \cdot T}\right), \quad (57)$$

where  $\tau_0$  is independent of temperature,  $R$  is the ideal gas constant, and  $E_A$  is the activation energy. Thus  $\ln(\tau_E)$  and  $E_A/R \cdot T$  are equivalent for a single relaxation time dielectric. In this case eq. (57) indicates that over the convenient temperature range from liquid nitrogen (77 K) to room temperature (300K), the retardation time can vary over a very large range. For an activation energy of 50 kJ/mol, for example,  $\tau$  changes by a factor of  $10^{25}$ , compared with  $10^8$  or so for conventional ac bridge techniques. The temperature variable has therefore been often used for scans of the total relaxation spectrum, and was frequently used for polymers, whose relaxation behavior is usually characterized by widely separated and very broad peaks. These experiments are increasingly rendered passé by modern wide frequency range relaxation spectrometers. Temperature scans are difficult to analyze quantitatively, however, and it is usually difficult to evaluate the dispersion ( $\epsilon_0 - \epsilon_\infty$ ) from temperature data because both  $\epsilon_0$ , and to a less extent  $\epsilon_\infty$ , are temperature dependent. Although this dispersion can be evaluated from the approximate relation [16]

$$(\epsilon_0 - \epsilon_\infty) \approx \left(\frac{2}{\pi \cdot R}\right) \cdot \left\langle \frac{1}{E_A} \right\rangle^{-1} \cdot \int_0^\infty \epsilon''(T) d(1/T) \quad (58)$$

The approximate nature of this relation derives from the assumption (made for mathematical tractability) that  $(\epsilon_0 - \epsilon_\infty)$  is independent of temperature [16], and that it is  $\langle E_A \rangle$  that is obtained in the frequency - temperature domain ("transition map") rather than  $\langle 1/E_A \rangle^{-1}$ , and it can be shown from the Schmidt inequality that

$$\langle E_A \rangle \cdot \langle 1/E_A \rangle > 1 \quad (59)$$

Finally, there are two situations where  $\ln(\omega)$  and  $E_A/R \cdot T$  are not equivalent variables. First, there is no equivalence for functions in which  $\omega$  and  $\tau_E$  are not invariably multiplied together (for example the conductivity of a Debye dielectric, eq. (46)). They are also not equivalent if the distribution of retardation times changes with temperature,

### 3.7 Determination of Activation Energies

The logarithm of frequency or the inverse temperature at which  $\epsilon''$  passes through its maximum can be plotted against the other and the activation energy determined from the slope:

$$\langle E_A \rangle = -R \cdot \left[ \frac{d \ln(f)}{d(1/T)} \right] \quad (60)$$

In some cases, however, the activation energy obtained in this way is ambiguous, depending on whether it is determined in the isothermal frequency domain or in the temperature domain at constant frequency. There is at least one explicit reference to this in the literature [17], where the frequency domain plot of  $\ln f_{\max}$  vs.  $1/T$  was found to be strongly curved whereas the plot of  $\ln f$  vs.  $1/T_{\max}$  was found to be linear.

## 4. CONDUCTIVITY RELAXATION

### 4.1 General Concepts and Basic Formalisms

Relaxation of polarization induced by an electric field can occur in two physically distinct ways: dielectrically by rotation of dipoles or by trapped ions oscillating between sites, and by conductivity relaxation [18] arising from long range translational migration of point charges. The relaxational character of conductivity is demonstrated by the existence of a relaxation time, the Maxwell relaxation time defined in eq. (21). From the definitions  $\epsilon' = C_p/C_0$  [eq. (30)] and  $\sigma' = e_0/(C_0 R_p)$  [eq. (31)] this Maxwell time is also given by

$$\tau_D = R_p \cdot C_p = \frac{e_0 \cdot \epsilon'}{\sigma'} \quad (61)$$

Note that this time is very different from the "relaxation time"  $\tau_e$  in the Fermi gas expression for electronic conductivity in metals, which is directly proportional to  $\sigma'$  [19]:

$$\tau_e = \frac{m \cdot \sigma'}{n \cdot e^2} \quad (62)$$

where  $n$  is the number density of charge carriers of effective mass  $m$  and charge  $e$ . The reason for the difference is that in the Fermi gas expression,  $\tau_e$  is the time between electron scattering events (collisions with ions or other electrons), whereas  $\tau_D$  is the residence time between jumps to and from adjacent sites. Formally, the Maxwell conductivity relaxation time is a measure of the rate of decay of the polarization at constant displacement, i.e. the decay of the electric field  $E$  at constant  $D$  [18] (hence the subscript  $D$ ). On the other hand, as noted already, the dielectric retardation time is a measure of the decay rate of the polarization at constant  $E$ , i.e. of  $D$  at constant  $E$  and has been referred to above as  $\tau_E$ . The two times are usually different, but are related by an expression to be discussed later [eq. (72)].

To analyze conductivity relaxation, it is helpful to describe it in terms of a function which exhibits the same sort of loss peak exhibited by  $\epsilon''$  for dielectric relaxation. The function  $\epsilon^*$  is not suitable, because  $\epsilon''$  for a frequency invariant conductivity exhibits a monotonic inverse proportionality to frequency [eq. (53)]. On the other hand, the two impedance functions, the electric modulus  $M^*$  [18] and complex resistivity  $\rho^*$  [20,21], are well suited for this purpose. The electric modulus was first defined by McCrum, Read and Williams [17], but its use in analyzing conductivity relaxation was first initiated and exploited by Macedo and coworkers [18].

The usefulness of  $M^*$  and  $\rho^*$  is illustrated by the simple system characterized by a frequency independent conductivity  $\sigma_0$  and relative permittivity  $\epsilon_\infty$  (the reason for the subscripts, which are superfluous here, will become clear when distribution functions are considered in section 5.2). The components of  $M^*$  are, in terms of the components of  $\epsilon^*$ :

$$M' = \frac{\epsilon'}{\epsilon'^2 + \epsilon''^2}, \quad (63)$$

$$M'' = \frac{\epsilon''}{\epsilon'^2 + \epsilon''^2}. \quad (64)$$

Insertion of the relation between  $\epsilon''$  and  $\sigma'$  [eq. (53)] and between  $\epsilon'$  and  $\sigma''$  [eq. (61)] into these equations yields

$$M' = \left( \frac{1}{\epsilon_\infty} \right) \left( \frac{\omega^2 \tau_D^2}{1 + \omega^2 \tau_D^2} \right) \quad (65)$$

and

$$M'' = \left( \frac{1}{\epsilon_\infty} \right) \cdot \left( \frac{\omega \cdot \tau_D}{1 + \omega^2 \cdot \tau_{D2}} \right) = \left( \frac{1}{\epsilon_\infty} \right) \cdot \text{sech}[\ln(\omega \cdot \tau_D)]. \quad (66)$$

Equation (66) is identical in form to eq. (44) for  $\epsilon''$ , so that  $M''$  exhibits the desired (symmetric) peak when plotted against  $\ln(\omega)$ . The components of  $\rho^*$  and  $M^*$  are related by

$$\begin{aligned} M' &= e_0 \cdot \omega \cdot \rho'' \\ M'' &= e_0 \cdot \omega \cdot \rho' \end{aligned} \quad (67)$$

Thus, in analogy with eq. (66) for  $M''$ ,  $\rho''$  is given by

$$\rho'' = \left( \frac{1}{e_0 \cdot \epsilon_\infty \cdot \omega} \right) \left( \frac{\omega^2 \tau_D^2}{1 + \omega^2 \tau_D^2} \right) = \rho_0 \cdot \left( \frac{\omega \tau_D}{1 + \omega^2 \tau_D^2} \right), \quad (68)$$

where

$$\rho_0 = \frac{1}{\sigma_0} = \left( \frac{\tau_D}{e_0 \cdot \epsilon_\infty} \right). \quad (69)$$

Equations (66) and (68) illustrate that  $M''$  and  $\rho''$  have the same frequency dependences, but are weighted by  $\epsilon_\infty^{-1}$  and  $\rho_0$ , respectively. This is an important difference, that in favorable circumstances can be exploited to considerable advantage (*vide infra*).

For dielectric relaxations,  $M^*$  and  $\epsilon^*$  are essentially equivalent because a dielectric relaxation that exhibits a peak in  $\epsilon''$  will also exhibit a peak in  $M''$ . Generally speaking,  $\epsilon'$  is usually significantly greater than  $\epsilon''$  for a dielectric relaxation, so that approximately

$$M'' = \left[ \frac{\epsilon''}{\epsilon'^2 + \epsilon''^2} \right] \approx \left[ \frac{\epsilon''}{\epsilon'^2} \right] = \frac{\tan \delta}{\epsilon'}. \quad (70)$$

Quantitatively, insertion of eqs. (43) and (44) into eq. (64) for  $M''$  yields [18,22]

$$M'' = (\epsilon_\infty^{-1} - \epsilon_0^{-1}) \cdot \left( \frac{\omega \cdot \tau_D}{1 + \omega \cdot \tau_D^2} \right) \quad (71)$$

where [18,22]

$$\tau_D = \left( \frac{\epsilon_\infty}{\epsilon_0} \right) \cdot \tau_E. \quad (72)$$

Although it would appear that a peak in  $M''$  could be due to either a conductivity or dielectric process, and that  $M^*$  could not distinguish between them, this is not always so. If the relaxation is due to conductivity, the relaxation time  $\tau_D$ , (or its average, see below) will be calculable from the limiting low frequency conductivity  $\sigma_0$ . An excellent example of dielectric relaxation

being correlated with  $\sigma_0$  occurs in the alkali silicate glasses, that originally led to the inference that the dielectric loss is due to the same alkali migration process that produces  $\sigma_0$  [7-13], and to which the modulus formalism and the concept of conductivity relaxation were first applied by Macedo and coworkers [18].

In the absence of electrode polarization, the low frequency behavior of  $M'$  is also different for dielectric and conductivity relaxations. For dielectrics  $M'$  behaves as

$$M' \rightarrow \epsilon_0^{-1} \text{ as } \omega \rightarrow 0, \quad (73)$$

that contrasts with  $M' \rightarrow 0$  as  $\omega \rightarrow 0$  for a conductivity relaxation [eq. (65)]. The last limit is conceptually important. The real part of the electric modulus is a measure of the restoring force in response to an electric field perturbation. This is finite for a dielectric relaxation, which can be interpreted as the charge storage ability (measured by  $\lim_{\omega \rightarrow 0} \epsilon_0$  remaining finite and  $\lim_{\omega \rightarrow 0} \epsilon'' \rightarrow 0$ ). For a conductivity relaxation the dielectric loss becomes infinite as  $\omega \rightarrow 0$ , and this dissipation completely overrides the storage capability. Thus no restoring force is observed and  $M' \rightarrow 0$  as  $\omega \rightarrow 0$ , analogous to the mechanical modulus going to zero as the viscosity of a viscoelastic material dominates at low frequency and the elasticity disappears. The electric modulus was first introduced to emphasize this mechanical analogy [17].

$$(74)$$

$$M'(\omega) = M_\infty \cdot \int_{-\infty}^{+\infty} \frac{g(\ln \tau_D) \cdot (\omega^2 \cdot \tau_D^2)}{1 + (\omega^2 \cdot \tau_D^2)} d \ln \tau_D \quad (75)$$

$$M''(\omega) = M_\infty \cdot \int_{-\infty}^{+\infty} \frac{g(\ln \tau_D) \cdot (\omega \cdot \tau_D)}{1 + (\omega^2 \cdot \tau_D^2)} d \ln \tau_D \quad (76)$$

and similarly for  $\rho^*$  and its components. However, there is an important distinction between the effects of a distribution of conductivity relaxation times and a distribution of dielectric retardation times. It is readily shown [18] that

$$\sigma_0 = \lim_{\omega \rightarrow 0} (\sigma^*) = \frac{e_0 \cdot \epsilon_\infty}{\langle \tau_D \rangle} = \frac{e_0}{M_\infty \cdot \langle \tau_D \rangle}; \quad (77)$$

$$\sigma_\infty = \lim_{\omega \rightarrow \infty} (\sigma^*) = e_0 \cdot \epsilon_\infty \cdot \langle 1/\tau_D \rangle = \frac{e_0 \cdot \langle 1/\tau_D \rangle}{M_\infty}; \quad (78)$$

and

$$\epsilon_0 = \lim_{\omega \rightarrow 0} (\epsilon^*) = \frac{\epsilon_\infty \cdot \langle \tau_D^2 \rangle}{\langle \tau_D \rangle^2} = \frac{\langle \tau_D^2 \rangle}{M_\infty \cdot \langle \tau_D \rangle^2}. \quad (79)$$

For conductivity relaxations, therefore, the dispersions in both conductivity and permittivity are determined by the breadth of the distribution function. This contrasts with dielectric relaxation, for which only the frequency range of the dispersion is affected by the distribution. The dependence of the dispersions in  $\epsilon^*$  and  $\sigma^*$  on the distribution function can be interpreted as follows [18]. The permittivities of most materials generally vary by a factor of 10 or less, so that a distribution in relaxation times is determined primarily by the distribution of conductivities in the sample. Since polarization occurs at the interface of two regions of differing conductivity, a greater spread of conductivities will produce increased polarization. It is for this reason that the impedance formalisms  $M^*$  and  $\rho^*$  are particularly useful for analyzing interfacial polarization.

Note that that a distribution in retardation times for  $\epsilon^*$  also produces a dispersion in  $\sigma^*$ :

$$\begin{aligned} \sigma_0 &= 0; \\ \sigma_\infty &= (\epsilon_0 - \epsilon_\infty) \cdot e_0 \cdot \langle 1/\tau_E \rangle. \end{aligned} \quad (80)$$

In modulus spectroscopy, a distribution of conductivity relaxation times cannot be distinguished in principle from dielectric and conductivity relaxations occurring together [18,22]. However, if the dielectric retardation time is much longer than the conductivity relaxation time, ( $\tau_E/\tau_D \gg 1$ ), then the dielectric relaxation will not be seen, because the value of  $\sigma_0$  will be much higher than the limiting high frequency dielectric loss conductivity  $\sigma_\mu(\infty)$ :

$$\frac{\sigma_0}{\sigma_\mu(\infty)} = \frac{\epsilon_\infty}{(\epsilon_0 - \epsilon_\infty) \cdot \langle \tau_D \rangle \cdot \langle 1/\tau_E \rangle}. \quad (81)$$

This phenomenon has been observed in systems for which the dielectric retardation time is essentially constant but whose conductivity is increased by addition of electrolyte [23,24]. These effects are ameliorated if conductivities can be measured with very high precision (see Schwan et al. [25], for example).

### **4.3. Electrode Polarization.**

The direct determination of the low frequency quantities  $\epsilon_0$  and  $\sigma_0$  is often made difficult, and sometimes rendered completely intractable, by the effects of electrode polarization.

#### **4.2 Distribution of Conductivity Relaxation Times.**

In direct analogy with eq. (49) for  $\epsilon^*$ ,  $M^*$  and  $\rho^*$  can also be described in terms of a distribution of relaxation times:

$$M^*(i \cdot \omega) = M_\infty \cdot \int_{-\infty}^{+\infty} \frac{g(\ln \tau_D) \cdot (i \cdot \omega \cdot \tau_D)}{1 + (i \cdot \omega \cdot \tau_D)} d \ln \tau_D$$

trode polarization. For materials which

are not electronic conductors and for which charge transport across the electrode interface is not significant (“blocking electrodes”), polarization can be approximately simulated by a pure capacitance  $C_s$  in series with the sample [26, 27, 49]. Strictly speaking a Faradaic impedance is in parallel with this, but for applied voltages which are below the decomposition potential of the material this can be neglected [27]. In this case it can be shown [18,22] that the imaginary component of the electric modulus is unaffected by electrode polarization provided that  $C_s$  is much larger than the sample capacitance (which is often the case), and that only the real part of the electric modulus is affected at low frequencies:

$$\lim_{\omega \rightarrow 0} M'(\omega) = \left( \frac{C_0}{C_s} \right) \quad (82)$$

This is a considerable advantage of the modulus formalism, since electrode polarization is a ubiquitous phenomenon. However, electrode polarization causes a rapid rise in  $\rho''$  at low frequencies:

$$\lim_{\omega \rightarrow 0} \rho'' \approx \frac{1}{\omega \cdot C_s} \quad (83)$$

Electrode polarization is usually characterized by two other low frequency effects, a rapid rise in  $\epsilon'$  and, at lower frequencies, a decrease in  $\sigma'$ . It is these effects that often prevent the observation of low frequency plateaux in  $\epsilon'$  and  $\sigma'$ . The dispersion in  $\epsilon'$  due to polarization occurs, generally, at much lower frequencies than the bulk dispersion:

$$\tau_{electrode} \approx \frac{\epsilon_0 \cdot C_s}{C_0 \cdot \sigma_0} \quad (84)$$

compared with

$$\tau_D \approx \frac{\epsilon_0 \cdot C_p}{C_0 \cdot \sigma_0} \quad (85)$$

When  $C_s \gg C_p$ , then clearly  $\tau_{electrode} \gg \tau_D$ . However, the magnitude of the polarization dispersion [proportional to  $(C_s - C_p) \approx C_s$ ] is correspondingly larger, so that the high frequency tail of the polarization dispersion extends well into the bulk relaxation region.

The phenomenon is perhaps best illustrated by a specific example. Consider the case where the low frequency bulk capacitance  $C_p \approx 10^{-11}$  F (10 pF), the electrode capacitance  $C_s \approx 10^{-8}$  F ( $10^4$  pF) and the bulk resistance  $R_p$  is  $10^7$  ohm. The bulk dispersion is therefore centered at ca.  $\omega \approx 1/(R_p C_p) \approx 10^4$  rad sec $^{-1}$ . For a typically broad bulk distribution function the low frequency plateau of  $\epsilon'$  will occur at ca.  $\omega \approx 10^2$  rad sec $^{-1}$ , at which frequency the

polarization gives a capacitance of about  $(\omega^2 \cdot R_p^2 \cdot C_s)^{-1} \approx 10^{-10}$  F (100 pF), an order of magnitude higher than the bulk capacitance. On the other hand, the low frequency dispersion in conductivity due to polarization has barely begun at  $\omega \approx 10^2$  rad sec<sup>-1</sup>, the decrease in conductivity being only ca. 1% since

$$\frac{\sigma_{electrode}}{\sigma_0} \approx \frac{\omega^2 \cdot \tau_{electrode}^2}{1 + \omega^2 \cdot \tau_{electrode}^2} \approx 0.99 \text{ for } \omega \cdot \tau_{electrode} \approx 10. \quad (86)$$

Note that since  $\tau_{electrode}$  is determined by  $C_s \cdot R_p$ , the high frequency conductivity for the electrode polarization dispersion is  $\sigma_0$  itself:

$$\begin{aligned} \sigma_{\infty}(electrode) &= \frac{(\epsilon_0 - \epsilon_{\infty}) \cdot e_0}{\tau_E} = \frac{(\epsilon_0 - \epsilon_{\infty}) \cdot e_0 \cdot \epsilon_{\infty}}{\tau_D \cdot \epsilon_0} = \frac{(\epsilon_0 - \epsilon_{\infty}) \cdot \sigma_0}{\epsilon_0} \\ &= \left( \frac{C_s - C_p}{C_s} \right) \cdot \sigma_0 \approx \sigma_0 \end{aligned} \quad (87)$$

for  $C_s \gg C_p$ . . . Effects similar to electrode polarization can arise from a number of other causes as well. One is poor contact between the electrode and the sample, which can result in a capacitance due to air gaps being in parallel with a conductance at the contact points. For example, air gaps and poor electrode contacts in general have been shown to give rise to spurious dielectric losses in undoped alkali halides [28] and is suspected to be responsible for the poor reproducibility of many reported dielectric losses in the alkali halides.[29]. Space charge effects can also give rise to a capacitance at the electrode [30] although it is generally smaller than a typical double layer capacitance.

If the applied voltage is too high electrolysis can occur and give rise to a Faradaic impedance in parallel with the double layer capacitance. The Faradaic impedance is usually taken to be a pure resistance due to electron transfer, which is voltage dependent, in series with the Warburg impedance [31] due to diffusion of the electrode products. The latter has a frequency dependence given by

$$\rho_W^* = \frac{(1-i) \cdot k_W}{\omega^{1/2}} \quad (88)$$

where  $k_W$  is a function of electrode product concentration and the diffusion coefficient [32]. The other functions for the Warburg impedance are

$$\sigma_W^* = \left( \frac{1}{2 \cdot k_W} \right) \cdot (1+i) \cdot \omega^{1/2} \quad (89)$$

$$\epsilon_W^* = \left( \frac{1}{2 \cdot e_0 \cdot k_W} \right) \cdot (1+i) \cdot \omega^{-1/2} \quad (90)$$

$$M_w^* = \sigma_w^* = \epsilon_0 \cdot k_w \cdot (1-i) \cdot \omega^{1/2} \quad (91)$$

The Warburg impedance can occur only when the concentration of mobile ions adjacent to the electrode is independent of the potential difference between the electrode and electrolyte and it is not possible if there is only one mobile species present, as occurs in most solid electrolytes. However, Bruinink and Broers [34] observed a Warburg like impedance in parallel with the bulk impedance in  $\text{KHF}_2$ , and attributed it to heterogeneities within the electrolyte. The effect was observed over a small range in frequency (a factor of 220). Consistent with this, Armstrong et al.[20] found it difficult to distinguish experimentally between a Warburg impedance and a rough electrode surface.

In complex plane plots of all four basic functions, the Warburg impedance gives a straight line of slope +1, since the real and imaginary components of all four functions have the same frequency dependence. The same occurs for any function which has a simple power frequency dependence,  $\omega^{\pm\alpha}$ , since it can be shown from the Kronig-Kramer relations that if one component of a complex function has such a frequency dependence then the other component has the same dependence. Also, the corresponding time domain functions can be shown to be proportional to  $t^{\mp\alpha}$ . A straight line in the complex plane does not necessarily indicate, however, that an electrode or other interfacial phenomenon is occurring. In fact, Jonscher [35] observes that such behavior is a common dielectric response shared by a large variety of materials, particularly at high frequencies, and has given a theoretical account of it [36], that has been generalized [37].

The effects of a Warburg impedance in a number of different circuit configurations have been described by Bauerle [38] in the complex admittance plane. In the complex impedance plane, a Warburg impedance in series with the bulk electrolyte gives a low frequency spike oriented at  $\pi/4$  to the real axis, analogous to the vertical spike of a pure capacitance. If a capacitance and Warburg element are in parallel and of comparable magnitude, the spike will make an angle between  $\pi/4$  and  $\pi/2$  with the real axis, and is therefore indistinguishable from the behavior of a rough electrode [38]. However, provided no large amount of curvature is present the same extrapolation procedure for obtaining the bulk resistance in the presence of a purely capacitive electrode impedance can be used.

#### **4.4 Illustration of Electrode Polarization and Bulk Relaxations in the Frequency Domain.**

A physical feeling for the relations given in the previous 3 subsections can be attained with the help of an idealized system consisting of the simple equivalent circuit given in Fig. 2a, and a geometric cell constant of  $1.0 \text{ cm}^{-1} = 0.01 \text{ m}^{-1}$ . The distribution function for this circuit consists of two single relaxation times  $\tau_1 = (10^8 \Omega) \cdot (10^{-12} \text{ F}) = 10^{-4} \text{ sec}$  and

$\tau_2 = (10^6 \Omega) \cdot (10^{-12} \text{ F}) = 10^{-6} \text{ sec}$ , respectively, corresponding to the two parallel *RC* elements.

Electrode polarization is simulated by the capacitance  $C_s$  in series with them. Such a circuit has been found to be quite successful in simulating the electric response of a variety of polycrystalline electrolytes, including an electronically semiconductor [40], a superionic conductor [20], and an average ionic conductor [41]. Generally speaking, one of the *RC* elements simulates the crystal impedance and the other *RC* element simulates any inter-granular

impedance.

The relaxation time averages are

$$\begin{aligned}\langle \tau_D \rangle &= \frac{(\tau_1 + \tau_2)}{2} = 5.05 \times 10^{-5} \text{ sec}; \\ \langle \tau_D^2 \rangle &= \frac{(\tau_1^2 + \tau_2^2)}{2} = 5.0005 \times 10^{-9} \text{ sec}^2; \\ \langle \tau_D^{-1} \rangle &= \frac{(\tau_1^{-1} + \tau_2^{-1})}{2} = 5.05 \times 10^{+5} \text{ sec}^{-1}\end{aligned}\tag{92}$$

The high frequency permittivity is

$$\epsilon_\infty = \frac{C_{\text{circuit}} \cdot C_s}{C_0 \cdot (C_{\text{circuit}} + C_s)} = \frac{(0.5 \times 10^{-12} \text{ F}) \cdot (10^{-6} \text{ F})}{(8.854 \times 10^{-14} \text{ F}) \cdot (10^{-6} \text{ F})} = 5.647,\tag{93}$$

and from eq. XXX for  $\epsilon_0$

$$\epsilon_0 = \epsilon_\infty \left( \frac{\langle \tau_D^2 \rangle}{\langle \tau_D \rangle^2} \right) = 5.647 \cdot \frac{(5.0005 \times 10^{-9})}{(5.05 \times 10^{-5})^2} = 11.07.\tag{94}$$

From eqs. XXX and YYY for  $\sigma_0$  and  $\sigma_\infty$ :

$$\sigma_0 = \frac{e_0 \cdot \epsilon_\infty}{\langle \tau_D \rangle} = \frac{(8.854 \times 10^{-12} \text{ F/m}) \cdot (5.647)}{5.05 \times 10^{-5} \text{ sec}} = 9.901 \times 10^{-9} \text{ S/m};\tag{95}$$

$$\begin{aligned}\sigma_\infty &= e_0 \cdot \epsilon_\infty \cdot \langle \tau_D^{-1} \rangle = (8.854 \times 10^{-12} \text{ F/m}) \cdot (5.647) \cdot (5.05 \times 10^{+5} \text{ sec}) \\ &= 2.525 \times 10^{-7} \text{ S/m}\end{aligned}\tag{96}$$

The frequency dependences of  $\sigma^*$  and  $\epsilon^*$  are given in Figs. 2b and 2c, and those of  $\rho^*$  and  $M^*$  are given in Figs. 2d and 2e. The corresponding complex plane plots are given in Figs. 3(a-d). There are a number of features in these figures that illustrate many of the observations made in previous sections, and these will now be discussed.

(1) The relative heights of the loss modulus and resistivity peaks are markedly different. This is a direct reflection of the different weighting of the two functions (eqs. XXX, YYY). For the particular values of the component circuit elements given in Fig. 2a the capacitances of the relaxing elements are the same and the two peaks in  $M''$  are equal in height. However the resistances differ and the lower resistance (higher frequency) relaxation gives a smaller peak in  $\rho''$ , which on the linear scale of Fig. 2d is not evident (see inset for logarithmic scale). If the parallel  $RC$  elements differed in capacitance instead, the two modulus peaks would

differ in height with the higher capacitance (lower frequency) relaxation being suppressed (e.g. Fig. 11b). This is discussed in detail in the literature [4], and as will be shown in the final section it is of considerable help in analyzing systems that contain high capacitance effects, such as are commonly encountered in systems containing thin inter-faces (e.g. intergranular impedances in polycrystalline solid electrolytes).

(2) After subtraction of the limiting low frequency conductivity contribution  $\sigma_0/(e_0 \cdot \omega)$  from the dielectric loss  $\epsilon''$ , and the infinite frequency capacitance contribution from the imaginary conductivity component  $\sigma''$ , both functions exhibit a single peak that lies between the modulus and resistivity peaks. This occurs because at intermediate frequencies the high frequency relaxation element behaves as a pure resistance and the low frequency elements behave as a pure capacitance, and as discussed in Section XXX this will give a dielectric loss peak in these two admittance formalisms

(3) The decrease in conductivity and increase in permittivity at low frequencies is due to the series capacitance. The simulated polarization is also responsible for the low frequency rise in  $\rho''$  [eq. XXX]. In the equivalent circuit the value of this capacitance has been chosen to ensure a clean separation between the simulated polarization effects and the bulk relaxations. As will be demonstrated in section XXX, however, considerable overlap occurs in a typical experimental situation.

(4) The complex plane plots shown in Fig. 3, although qualitatively useful, are generally less informative than the spectra shown in Figs. 2. For example, it is difficult to compare the relative positions of the peaks in  $M''$  and  $\rho''$  because frequency increases in opposite directions in the two complex plane plots. In some situations, however, complex plane plots are preferable. For example, the complex resistivity plane is extremely useful for estimating  $\sigma_0$  in the presence of severe polarization [20]. (See section XXX dealing with methods of estimating  $\sigma_0$  in the presence of polarization and other effects). The spike in the resistivity plane, Fig. 3c, is due to the simulated electrode polarization. It occurs because each  $RC$  relaxation shows up in the complex plane as a semicircle with radius  $R$ , and the pure series capacitance has an infinite resistance and radius. The zero frequency conductivity also shows up as a spike, in this case in the complex permittivity plane. It corresponds to the infinite conductivity dielectric loss at zero frequency, discussed above in section XXX

(5) The increase in conductivity above its low frequency plateau level occurs at a frequency that corresponds closely to the inverse average relaxation time (arrowed Fig. 2b). This is often observed in experimental data as well, and in cases where the plateau is reasonably well defined it is possible to determine if the rise is due to a conductivity relaxation. If it is, then the angular frequency  $\omega_{crossover}$  at which the rise occurs is related to the plateau conductivity  $\sigma_0$  by the relation

$$\omega_{crossover} \approx \frac{\sigma_0}{e_0 \cdot \epsilon_\infty} \quad (97)$$

which is obtained by putting  $\omega \cdot \tau_d \approx 1$ . In the absence of specific data,  $\epsilon_\infty$  may be put equal to 7 in this expression.

#### 4.5 Determination of Zero Frequency Conductivity from ac Data.

Because of polarization and other effects (such as those due to intergranular impedances in polycrystalline preparations) the low frequency plateau in the conductivity at  $\sigma_0$  seen in Fig. 2b is often not observed in experimental data. However, there are several methods which can be used to make a reasonable estimate of  $\sigma_0$ , and these are discussed here at some length. Before this, however, the importance of a correct determination of  $\sigma_0$  and some of the spurious effects resulting from an incorrect determination will be illustrated.

If  $\ln \sigma$ , taken at a fixed frequency, is plotted as a function of  $1/T$  in the usual Arrhenius plot, spurious breaks in the curve can result from polarization and bulk relaxation effects. If the measuring frequency lies in the region where, at a particular temperature, polarization is important then the measured conductivity is lower than  $\sigma_0$ , by an amount which increases with increasing temperature because of the shift to higher frequencies of the polarization phenomenon. This results in a lower observed activation energy at high temperatures which is quite spurious. Similarly, if the measuring frequency lies in the bulk relaxation region the measured conductivity exceeds  $\sigma_0$ , by an amount which decreases with increasing temperature. This also results in a spuriously low apparent activation energy, but in this case the deviation occurs at low temperatures. Both these phenomena are illustrated in Fig. XXX.

In extreme cases where the high frequency conductivity is directly proportional to frequency raised to a power near unity, such as occurs in electronic amorphous semiconductors [42], the fixed frequency conductivity will become nearly independent of temperature at low temperatures. This has been observed by Le Cleach and Palmier [43] for example, and occurs because a change in temperature which increases the conductivity by an order of magnitude at all frequencies also shifts the conductivity spectrum to higher frequencies by an order of magnitude, thus moving a lower frequency-lower conductivity point up to the measuring frequency.

An accurate determination of  $\sigma_0$  is also required if relaxation data are analyzed in terms of the complex permittivity, where  $\sigma_0$  must be subtracted before data processing is done. This has been pointed out above, and the difficulties encountered have recently been illustrated explicitly by Ravaine and Souquet [44].

##### 4.5.1 Use of the Complex Resistivity Plane.

The use of the complex resistivity plane (or the complex impedance plane), for determining  $\sigma_0$  in the presence of severe polarization, has been used extensively by Armstrong et al. [41]. The principle of the method is to extrapolate the polarization spike (as in Fig. 3c, for example) to the  $\rho'$  axis, and to equate  $\rho_0 = 1/\sigma_0$  with the intercept. In many cases the spike occurs at an angle with the  $\rho'$  axis, and this has been attributed to surface roughness at the electrode interface [38]. Curvature of the spike is also sometimes observed. As mentioned in Section XXX, this is expected if the Faradaic impedance which is in parallel with the capacitance has a significant resistive component at the measuring frequency and voltage. Experimental examples of the technique are given in Section XXX.

The complex resistivity plane has also been used by Ravaine and Souquet [44] for obtaining  $\sigma_0$  for alkali silicate glasses in the presence of mild electrode polarization. In this case the high frequency complex resistivity spectrum is fitted to the Cole-Cole function (see

Appendix XXX), and the low frequency spectrum is determined by extrapolation of the semicircle in the complex plane.

#### **4.5.2 Modulus and Resistivity Spectra**

In cases where polarization and bulk relaxation effects overlap to the extent that no plateau in  $\sigma$  is observed,  $\sigma_0$  can be calculated from eq. if  $\langle \tau_D \rangle$  and  $\epsilon_\infty$  are known. The latter two quantities can often be found by fitting the imaginary component of the electric modulus,  $M''$ , to some empirical function. As explained in 3.3,  $M''$  suppresses high capacitance effects such as those due to polarization so that only the bulk relaxation is included in the fitted function. Both  $\langle \tau_D \rangle$  and  $\epsilon_\infty$  can be calculated from the parameters of the best fit function. Although somewhat tedious, this method is capable of yielding quite accurate results. It is demonstrated in detail in Section XXX.

The maximum in  $\rho''$ ,  $\rho''_{\max}$ , can also be used to estimate  $\sigma_0$ . If the half width of the peak in  $\rho''$  is  $\Delta$  decades (e.g. 1.14 for a Debye curve), the value of  $\sigma_0$  can be estimated to within  $\pm 10\%$  or so from the relation

$$\sigma_0 \approx \frac{1}{1.75 \cdot \Delta \cdot \rho''_{\max}} \quad (98)$$

If only one side of the peak is observable, it is still possible to estimate  $\sigma_0$  by assuming the peak in  $\rho''$  to be symmetric. With the same assumption of symmetry  $\sigma_0$  may also be obtained from the value of  $\rho'$  at the angular frequency  $\omega_{\max}$  of maximum  $\rho''$

$$\sigma_0 = \frac{1}{2 \cdot \rho'(\omega_{\max})} \quad (99)$$

Both of these methods are essentially the spectral equivalents of the complex resistivity plane method used by Ravaine and Souquet [44] (Section XXX).

### **5. Applications of A.C. Formalisms to Experimental Data.**

It is an unfortunate fact that the frequency dependences of both  $\sigma'$  and  $\epsilon'$  are rarely both reported in the literature together as a function of frequency. In those cases where both are given the data are, of course, displayed graphically so that it is difficult to obtain accurate data from most publications for further processing. For these reasons many of the illustrative examples in this section are from the author's own work, although many of the details are given here for the first time.

#### **5.1 Applications of the Complex Admittance Formalism to Polycrystalline Electrolytes and Electrode Phenomena.**

One of the first uses of complex plane plots was in the analysis of polycrystalline yttria-zirconia electrolytes by Bauerle [38]. He gives an extensive discussion of equivalent circuits and their corresponding complex admittance plane plots. We will restrict our attention here to

the equivalent circuit used by Bauerle in the analysis of his data. It is given in Fig. 5a, and the corresponding complex admittance plane plot is given in Fig. 5b.

In the equivalent circuit one of the parallel  $RC$  elements represents the electrode interface, the capacitance being essentially due to a double layer and the resistance to an oxygen-gas – oxide ion charge transfer process [37]. The other  $RC$  element represents grain boundary (“constriction”) [37] impedances, and the sample resistance is the bulk resistance. The experimentally observed complex admittance plane plots were in excellent agreement with the equivalent circuit’s predicted admittance plane behavior (Fig.5c). Furthermore the limiting zero frequency conductivity predicted from the complex plane plot was in excellent agreement with separate 4-terminal conductance data [37], and the expected dependence of the electrode impedance on such things as oxygen partial pressure was observed.

For a system as complex as this, this is an impressive correlation. However, a number of caveats should be pointed out. First, in assuming that the bulk material acts as a pure resistance the analysis automatically assumes that the measuring frequencies are well below the conductivity relaxation frequency. This can, in general, only be confirmed retrospectively by demonstrating that the derived value of  $R_3$  is sufficiently low. Second, if one places a capacitance in parallel with  $R_3$  due to the bulk material there are clearly three relaxing elements in the circuit. The complex admittance, however, exhibits only two semicircles which reflect the *differences* between the relaxing elements. Third, if the observed relaxations overlap an assumption has to be made about the shapes of the two relaxations before extrapolations can be made. For example, it might have to be assumed that both relaxations can be described by the Cole-Cole function, with the centers of the complex plane semicircles lying below the real axis. This was the case for Bauerle’s data and an accurate analysis was accomplished, but this would not be expected to occur in general.

On the other hand, spectra of the electric loss modulus  $M''$  and resistivity  $\rho''$  would, in principle, exhibit three peaks corresponding to the three relaxations, from which the values of each  $R$  and  $C$  could be determined directly if overlap was not too great. A detailed comparison of the relative merits of this method over complex admittance and complex permittivity methods has been given in Section XXX.

## **5.2. Conductivity Relaxations in Homogeneous Materials.**

### **5.2.1. Analysis of Conductivity Relaxation in Glasses Using the Modulus and and Resistivity Formalisms.**

A convenient illustration of the use of the complex modulus and complex impedance formalisms can be made with the data of Hodge and Angell [45] on glassy aqueous acids. Although these electrolytes are rather unusual chemically their conductivity relaxation behavior is almost indistinguishable from other glassy conductors such as the alkali silicates [45].

The observed frequency dependences of  $\sigma'$  and  $\epsilon'$  for one of the glasses are shown in Fig. 6a. Features of interest are the absence of plateaux in both  $\sigma'$  and  $\epsilon'$  at low frequencies, and the continuous increase in  $\sigma'$  with increasing frequency. The solid lines are derived from the best fit Davidson-Cole function for the electric loss modulus  $M''$ , and are discussed below.

The electric loss modulus spectrum  $M''(\omega)$ , and that of the imaginary component of the resistivity  $\rho''(\omega)$ , are given in Figs. 6a and 6b respectively. The loss modulus spectrum is seen to be characterized by a long high frequency tail, that is described reasonably well by the

Davidson-Cole function (solid line in Fig 6a). For the purposes of illustration, the technique for fitting this particular function is now described in detail. The peak height,  $M''_{\max}$  and width at half height ( $\Delta$ ), can be determined quite accurately, to about  $\pm 2\%$  or so. The Davidson-Cole parameters  $\gamma$  (that determines  $\Delta$ ) and  $M_\infty$  (which, together with  $\Delta$ , determines  $M''_{\max}$ ) can therefore be calculated from the expressions given in Appendix XXX. It should be noted, however, that for a spectrum as wide as that observed in this case the value of  $\Delta$ , and more especially  $\gamma$ , is quite sensitive to the value  $M''_{\max}$ . Thus, great care is needed to ensure that an accurate determination of the latter is made. The value of the Davidson-Cole parameter  $\tau_0$  is determined by the frequency,  $f_{\max}$ , at which  $M''_{\max}$  occurs, or the upper frequency at which the spectrum falls to  $M''_{\max}/2$ . In this particular case, there is considerable uncertainty in  $f_{\max}$  because of the relatively wide spaced frequency increments (the reason for this is given in the original paper, and need not be of concern here). However,  $\tau_0$  can be determined quite accurately by the two frequencies at which the spectrum attains a value of  $M''_{\max}/2$ , particularly by the higher frequency  $f_{1/2}^+$ , from the expressions given in Appendix XXX.

In principle, the Davidson-Cole parameters could also have been obtained from the high frequency data in complex plane plots [46]. In this case, however, the observed high frequency data lay significantly above the Davidson-Cole function, thus invalidating the complex plane relations.

The frequency dependence of  $\sigma'$  and  $\epsilon'$  according to the Davidson-Cole function for  $M''$  and  $M'$  can be calculated from the inverses of eq. XXX, as follows:

$$\begin{aligned}\sigma' &= e_0 \cdot \omega \cdot \epsilon'' = e_0 \cdot \omega \cdot \left( \frac{M''}{M'^2 + M''^2} \right); \\ \epsilon' &= \left( \frac{M'}{M'^2 + M''^2} \right)\end{aligned}\tag{100}$$

The values of  $\sigma_0$ ,  $\epsilon_0$  and  $\epsilon_\infty$  can also be evaluated directly from the Davidson-Cole parameters, as follows (see Appendix XXX for relevant equations):

$$\sigma_0 = \frac{e_0}{M_\infty \cdot \langle \tau_D \rangle} = \frac{e_0}{M_\infty \cdot \gamma \cdot \tau_0} = 2.39 \times 10^{-7} \text{ S/m}\tag{101}$$

$$\epsilon_\infty = \frac{1}{\epsilon_\infty} = 9.52\tag{102}$$

$$\epsilon_0 = \epsilon_\infty \cdot \left( \frac{\langle \tau_D^2 \rangle}{\langle \tau_D \rangle^2} \right) = \epsilon_\infty \cdot \frac{1 + \gamma}{2 \cdot \gamma} = 19.1\tag{103}$$

The Davidson-Cole  $\sigma'$  and  $\epsilon'$  spectra, calculated from eqs. XXX and YYY, are shown as solid

lines in Fig. 6a. They illustrate clearly the suppression by the modulus formalism of the low frequency high capacitance polarization relaxation.

The calculated value of  $\sigma_0$  is seen to be close to the inflection point of the conductivity spectrum. This occurs: quite frequently, judging from (limited) published data. The inverse average relaxation time  $1/\langle\tau\rangle$  is also seen to be close to the radial frequency at which departures from the (calculated) plateau value of  $\sigma$  begin to be significant, that indicates that the dispersion in  $\sigma$  is due primarily to a conductivity relaxation (eq. XXX). The deviations at high frequencies are due to the experimental values of  $M''$  exceeding the Davidson-Cole fit. As discussed elsewhere [24, 45], this is believed to be due to a high frequency dielectric relaxation.

The resistivity spectrum of this material is shown in Fig. 6c. The severe polarization, evident in the  $\sigma'$  and  $\epsilon'$  data, is also reflected in the  $\rho''$  spectrum. In fact, the effects are so severe that it is not possible to extract useful information from the spectra. The complex resistivity plane is also of limited use (Fig. 6c). If the polarization "spike" is extrapolated to the  $\rho'$  axis, a value for  $\sigma_0$  of  $3.2 \times 10^{-7}$  S/m is obtained. Comparison with the  $\sigma'$  spectrum indicates that this is quite unreasonable. The reason for the failure in this case is that the data do not extent to low enough frequencies. The polarization is also too close to the bulk relaxation for the method of Ravaine and Souquet [44] to be used unambiguously. However, for the purposes of illustrating the latter method, the  $\rho''$  spectrum can be calculated from the Davidson-Cole fit to the modulus spectrum, which is shown as the solid curve in Figs. 5c and 5d.

The calculated  $\rho''$  spectrum is reasonably well fitted by the Cole-Cole function [47]. However, it should be pointed out if  $\rho^*$  conforms exactly to a Cole-Cole function then the modulus spectrum has pathological properties e.g.  $M'' \rightarrow \infty$  as  $\omega \rightarrow \infty$  [78]:

The Cole-Cole function for  $\rho'$  is

$$\rho' = \frac{\rho_0 \cdot [\sin(\alpha \cdot \pi / 2) + (\omega \cdot \tau_0)^{\alpha-1}]}{[2 \cdot \sin(\alpha \cdot \pi / 2) + (\omega \cdot \tau_0)^{1-\alpha} + (\omega \cdot \tau_0)^{\alpha-1}]} \quad (104)$$

As  $\omega \rightarrow 0$ , this becomes (since  $0 < \alpha \leq 1$ )

$$\lim_{\omega \rightarrow 0} \rho' = [\sin(\alpha \cdot \pi / 2)] \cdot (\omega \cdot \tau_0)^{\alpha-1} \quad (105)$$

and

$$\begin{aligned} \lim_{\omega \rightarrow \infty} M'' &= \lim_{\omega \rightarrow \infty} e_0 \cdot \omega \cdot \rho' = e_0 \cdot \omega \cdot \rho_0 \cdot \sin(\alpha \cdot \pi / 2) \cdot (\omega \cdot \tau_0)^\alpha \cdot \tau_0^{-1} \\ &\rightarrow \infty \text{ as } \omega \rightarrow \infty \end{aligned} \quad (106)$$

Thus the Cole-Cole function is nonsensical when applied to resistivity data. However, it is possible that another function which is experimentally indistinguishable from the Cole-Cole distribution does not have this pathological consequence. The present data suggest quite

strongly, for example, that a Davidson-Cole distribution in  $M^*$  is almost equivalent to a Cole-Cole distribution in  $\rho^*$  (See Appendix XXX for confirmation).

There is some doubt, however, whether or not the resistivity spectrum predicted from the Davidson-Cole function for  $M^*$  is appropriate in this case. It is quite possible, in principle, that some bulk relaxation information is being suppressed by  $M^*$  that might contribute to  $\rho^*$ . However, Ravaine and Souquet [12, 44] have found that the Cole-Cole function fits  $\rho^*$  data for alkali silicate glasses quite well, and it has been demonstrated by Hodge and Angell that the Davidson-Cole function also fits  $M^*$  data for similar alkali silicate glasses quite well. Thus, for the purposes of discussion and illustration, we shall assume that the derived  $\rho''$  spectrum reflects the full bulk relaxation spectrum.

The expression for estimating  $\sigma_0$  from the  $\rho''$  spectrum (eq. XXX), can be illustrated by this example. Of course, since the  $M''$  spectrum from which  $\rho''$  is derived also gives the correct  $\sigma_0$ , it can be asserted quite correctly that this is simply demonstrating self consistency. However, eq. XXX is a general expression which makes no assumption about the form of the distribution function for  $\rho^*$ , so that it is quite appropriate to test it in this case. The half-width of the derived  $\rho''$  spectrum is 1.25 decades, and its maximum is ca.  $1.9 \times 10^8$  ohm cm. When inserted into eq. XXX those values give an estimate of  $\sigma_0$  of ca. XXXX, compared with  $2.37 \times 10^{-7}$  S/m from the modulus spectrum. Extrapolation of the Cole-Cole arc in the complex resistivity plane (Fig. 6d) gives a value for  $\sigma_0$  of  $2.4 \times 10^{-7}$  S/m.

To summarize, it is apparent that electrode polarization in this particular set of data is quite severe, but that its effects can be usefully suppressed by the  $M^*$  formalism. The nature of the polarization process, e.g. to what extent it can be simulated by a pure capacitance, is best studied with the  $\rho^*$  formalism. The two formalisms are therefore complementary, and enable different features of the total relaxation spectrum to be projected at will.

### **5.2.2. Conductivity Relaxation in Single Crystal Beta Alumina.**

The impedance spectra ( $M''$  and  $\rho''$ ) of single crystal beta alumina at the low temperature of  $-160^\circ\text{C}$  have been measured and analyzed by Grant and Ingrain [48,60]. They compared the modulus spectra of single crystal  $\beta$ -alumina in orientations perpendicular and parallel to the conductance plane with the impedance spectrum of the parallel orientation and the dielectric loss spectrum in the perpendicular direction. The spectra are shown in Fig. 7, from which it can be seen that the parallel impedance spectrum peaks at about the same frequency as the perpendicular modulus and dielectric loss spectra.

The activation energy of the parallel impedance spectrum ( $18.4 \text{ kJ mol}^{-1}$ ) was found to be comparable with that of the perpendicular dielectric loss spectrum ( $16.2 \text{ kJ mol}^{-1}$ ). The authors suggested that in the perpendicular orientation sodium beta alumina was a classic Maxwell layered dielectric [64] with the spinel blocks acting as the dielectric layers and the conduction planes acting as the conductors. The activation energy for the dielectric loss is thus determined by the conductivity of the conducting layers, which the data suggest is similar in directions parallel and perpendicular to the conduction planes.

The enormous width of the modulus spectrum for single crystal sodium beta alumina in the parallel orientation [60, 61] is suggestive of a very wide distribution of relaxation times.

The impedance and modulus spectra together suggest that this width may be due to an essentially bimodal distribution function. Grant and Ingram suggested that, at the low temperature for which their data apply ( $-160^{\circ}\text{C}$ ), the low frequency conductivity is determined by an activated localized ion motion which is either the same in both orientations or is perpendicular to the conduction plane. The higher frequency conductivity, which contributes to the modulus spectrum but not to the impedance spectrum, results from a relatively free motion of the activated ions which is characterized by a low activation energy. It therefore appears that these workers have achieved a remarkable experimental separation of the rattle and jump components of the classical conductivity mechanism. Although not mentioned by these authors, this mechanism is also consistent with the low temperature localization of sodium ions deduced from nmr measurements.[66] At higher temperatures, the localized activation is not the rate determining step and the well known low activation energy for conductivity in sodium beta-alumina results.

This work is an excellent demonstration of the fine detail which can be deduced from experimental data if the correct formalisms are used. The deductions discussed above could certainly not have been made with the raw conductivity and permittivity data alone.

### **5.3 Analysis of interfacial Relaxation**

#### **5.3.1 Electrode Effects**

It will be assumed in the following discussion that the applied voltage is below the lowest decomposition potential for the electrode and electrolyte being studied. Thus the electric response characteristics of electrochemical reactions at the electrode will not be considered here; a review (for aqueous solutions) is in the literature [49].

Generally speaking, electrode polarization is characterized by a high capacitance which is in series with the bulk sample. The series circuit indicates that an analysis in terms of impedance formalisms such as the complex electric modulus or complex resistivity is preferable to that of admittance formalisms such as the complex permittivity or conductivity. Since the electric modulus formalism suppresses high capacitance phenomena (Sec 3.3XXX), it is the complex impedance or complex resistivity that is more generally useful. If electrode polarization is a problem only at the low frequency end of an experimentally accessible range then, generally speaking, it may be effectively suppressed by use of the electric modulus formalism. However, if polarization dominates most of the accessible frequency range and it is desired to make high frequency extrapolations to obtain data relating to the bulk sample then the complex impedance plane or impedance spectrum are best used. This section is devoted primarily to such methods of extrapolation.

#### **5.3.1 (i) Complex Impedance Plane Analysis of Electrode Polarization in Sintered $\beta$ -Alumina.**

The use of the complex plane in extrapolating polarization phenomena to get bulk data has been used extensively by Armstrong and coworkers [41] in their studies of superionic conductors such as sodium beta alumina [38,41] and silver rubidium iodide [20, 50-53], and some illustrative examples taken from their work are shown in Fig. 8. Ideally a pure capacitance at the electrode interface will give a vertical spike in the complex impedance plane (see sections XXX 3.3-3.5 and Fig. 3c). In practice, the spike usually occurs at some angle to the real axis (Fig. 8a) and in many cases is curved (Fig. 8b).

The sloping straight lines have been ascribed to surface roughness at the electrode [38]. Curvature of the spikes may be due to a Warburg impedance [20] and/or a Faradaic charge transfer resistance in parallel with the polarization capacitance. As seen in Fig. 8b, however, the curvature, if present, is small and reasonable extrapolations can still be made.

Also illustrated in Fig. 8b is the case where the polarization spike overlaps significantly with the semicircle associated with a parallel  $RC$  element (usually corresponding to the bulk impedance, including intergranular effects in polycrystalline solid electrolytes). Note that the different surface preparations affect the overall impedance spectra quite significantly, but that all of the extrapolations give the same value of  $\sigma_0$ .

Electrode polarization also manifests itself as a rapidly rising low frequency increase in spectra of  $\rho''$ . An example of this and its relation to the impedance plane spike has been given above in section XXX4.2, and will not be discussed further here.

### **5.3.1.(ii) Complex Impedance Plane Analysis of Atmosphere Dependent Electrode Effects in $\alpha$ - and $\beta$ -KHF<sub>2</sub>.**

Another excellent example of complex impedance plane analysis is found in the thorough study of both phases of KHF<sub>2</sub> by Bruinink and Broers [34,35]. In an atmosphere of hydrogen gas with platinum paint electrodes, the complex plane plot of data for  $\alpha$ -KHF<sub>2</sub> was consistent with a Warburg impedance (sec XXX3.3) in parallel with the bulk resistance and capacitance [54], and extrapolation to the real  $\rho'$  axis gave a value of  $\sigma_0$  in agreement with the separately determined dc value. This is shown in Fig. 9a. The plot gives no indication of interfacial polarization, consistent with the conclusion that  $\alpha$ -KHF<sub>2</sub> is a proton conductor and that the platinum paint electrodes were ideally reversible hydrogen electrodes with no associated polarization. This contrasts with the low frequency behavior of  $\alpha$ -KHF<sub>2</sub> in a vacuum, shown in Fig. 9b. Here a double layer capacitance of ca.  $44 \mu\text{F cm}^{-2}$  per electrode in parallel with a Faradaic resistance of ca.  $2 \times 10^4 \Omega / \text{cm}^2$  per electrode gives rise to an extra semi-circle in the complex plane. (The value of the resistance was obtained from the maximum value of  $Z''$ , and the capacitance from the frequency at which  $Z''$  passes through its maximum). For the  $\beta$  phase, which was polycrystalline, the complex plane plot given in Fig. 9c was observed. The plot was essentially the same for data taken in both a H<sub>2</sub> atmosphere and a vacuum [54]. It is consistent with a Warburg type impedance in series with an  $RC$  element corresponding to an interfacial polarization, the latter being due to blocking of  $\text{K}^+$  and/or  $\text{F}^-$  charge carriers at the electrode.

### **4.3.2 Intergranular Effects in Polycrystalline Electrolytes**

The effect of intergranular material on the overall electrical response of polycrystalline electrolytes is discussed here in detail. An account of the method described here has been given in full elsewhere [40,56], to which the reader is referred for experimental details.

The simplest representation of an intergranular impedance between grains in a polycrystalline preparation is the circuit given in Fig. 3a, where one  $RC$  element is associated with a grain, and the other with the inter-granular interface. It has been shown by Armstrong et al [20] that such a series circuit can represent the principle features of a polycrystalline electrolyte.

The values of the individual components, however, must differ from those given in Fig.

3a. Since the interface is thin and has a cross-section area that is less than the electrical pathways through the grains themselves, and because the permittivities of most materials vary by a factor of ca. 10 at most, the capacitance  $C_i$  associated with the interface is much higher than that of the grain;  $C_p$  :

$$C_i = \frac{\epsilon_0 \cdot \epsilon' \cdot A_i}{\ell_i} \gg C_p = \epsilon' \cdot C_0, \quad (107)$$

where  $A_i$  is the cross section area,  $\ell_i$  is the effective thickness of the interface, and  $C_0$  is the cell capacitance. Since intergranular resistances are a problem only when they are larger than those of the grains themselves, the interfacial resistance  $R_i$  will henceforth be assumed to be greater than that of a typical grain. Thus both the capacitance and resistance of the intergranular material will be greater than those of the grains themselves. This is illustrated schematically in Fig. 10a. As before (Fig. 2), the resistivity and modulus spectra reflect primarily the high resistance and low capacitance aspects, respectively, of the total electrical response.

#### **4.3.2.(i) Intergranular Cracking.**

Experimental  $M''$  and  $Z''$  spectra for a polycrystalline material known to have intergranular cracking [40] are shown in Figs. 10b and 10c. The similarity to the response of the simple equivalent circuit is quite clear, although the experimental peaks are broader. To a rough approximation the broader peaks can be described by the sum of two Debye peaks of equal heights, so that the maxima in  $Z''$  and  $M''$  may be put equal to  $R/4$  and  $C_0/4C$  respectively, rather than the values of  $Z'' = R/2$  and  $M'' = C_0/2C$  appropriate for a single Debye peak. The values of  $R$  and  $C$  for the intergranular and granular material calculated in this way, assuming the plausible resolution into symmetric  $\rho''$  peaks given in Fig. 10c, are:

*Intergranular (lower frequency) Relaxation:*

$$\tau_i = R_i \cdot C_i = \frac{1}{\omega_{\max}(Z'')} = 6.4 \times 10^{-6} \text{ sec}; \quad (108)$$

$$R_i = 4Z''_{\max} = 6.4 \times 10^6 \text{ ohm}$$

Thus

$$C_i = \frac{\tau_i}{R_i} = 1.0 \times 10^{-12} \text{ F} = 1.0 \text{ pF}. \quad (109)$$

*Granular (higher frequency) Relaxation*

$$\tau_g = R_g \cdot C_g = \frac{1}{\omega_{\max}(Z'')} = 1.6 \times 10^{-7} \text{ sec}; \quad (110)$$

$$R_g = 4Z''_{\max} = 2.6 \times 10^6 \text{ ohm}$$

$$\text{Thus } C_g = \tau_g / R_g = 6.12 \times 10^{-14} \text{ F} = 0.061 \text{ pF}.$$

After the intergranular cracking in this sample was annealed out by chemical reaction [40], the impedance spectrum was altered drastically (Fig. 10c). This spectrum is almost indistinguishable from the high frequency resistivity peak in the cracked material, strongly suggesting that it is due to relaxation in the grains themselves. The modulus spectrum is almost unaffected by the annealing, indicating that it is not influenced by the intergranular cracking which gave the second low frequency peak in the impedance spectrum.

Since the overall conductivity of the cracked sample is determined by the high resistance intergranular cracks, the ratio of the conductivities of the sample before and after annealing (Fig. 10d) should be the same as the relative heights of the two impedance peaks in the cracked sample. To within 10% or so this is found, thus justifying the use of a circuit such as that given in Fig. 10c in the analysis of the data. Finally, it should be emphasized that the detailed information about the resistivity and capacitance of the intergranular and intragranular relaxations that is deduced here could not have been obtained, even approximately, from the raw  $\sigma'$  and  $\epsilon'$  data (Fig. 10d). Modulus and impedance spectroscopy thus show up complexities in the electrical response whose existence may not even be suspected from the conventional  $\log \sigma'$  and  $\epsilon'$  vs  $\log f$  plots.

#### **4.3.2. (ii) Intergranular Gas Adsorption**

The effects of oxygen and alkali doping on the electric response of polycrystalline zinc oxide have been studied by Seitz and Sokoly [57]. Their conductivity and permittivity data were plotted as a function of frequency, thus permitting the modulus and resistivity functions to be calculated, albeit with large uncertainties due to reading errors of ca. 5% in  $f$ ,  $\sigma'$  and  $\epsilon'$ . The uncertainties in  $M''$  and  $\rho''$  are thus of the order 15% or so.

The original data for undoped polycrystalline zinc oxide exposed to an oxygen pressure of 1 atmosphere at 500 K is given in Fig. 11 (insert), and the derived resistivity and modulus spectra are given in Fig. 11 itself. The authors concluded, from the increase in conductivity with decreasing oxygen pressure and the absence of changes due to different electrode materials, that adsorbed oxygen at grain surfaces was responsible for the observed polarization of the sample.

The modulus and resistivity spectra, which both show two partially resolved peaks, are consistent with a thin, high resistance layer determining the low frequency electrical response. Both the low and high frequency peaks in  $M''$  appear to have comparable half-widths (ca. 1.5 decades), so that the relative heights ( $8 \times 10^{-4}$  and  $1.1 \times 10^{-2}$ ) are a good measure of the relative capacitances of each relaxation. Thus the capacitance of the low frequency relaxation is ca. 14 times larger, and from the frequencies at which the relaxations occur (ca. 500 and  $10^6$  Hz) it can be deduced that the resistivity of the low frequency process is ca. 140 higher. The conductivity evaluated from the height of the low frequency resistivity peak via eq. XXX is  $1.1 \pm 0.2 \times 10^{-5}$  S/m, in agreement with the observed low frequency plateau value of  $1.3 \pm \times 10^{-5}$  S/m. From the relative positions of the modulus peaks, and the relative heights of the (poorly resolved) impedance peaks, the conductivity of the high frequency relaxation is estimated to be between  $10^{-4}$  and  $10^{-3}$  S/m. Because of its higher capacitance the low frequency relaxation probably corresponds to an intergranular impedance, and its removal, e.g. by a reduction in oxygen partial pressure, should therefore increase the sample conductivity by ca.

140 and decrease the permittivity by ca. 14. These figures are in agreement with the stated increase in conductivity and reduction in permittivity with decreasing oxygen pressure, although the magnitude of these changes was not given in the original paper. However, with increasing temperature the intergranular oxygen is desorbed, and since permittivities are relatively weak functions of temperature it is possible to estimate the measured permittivity in the absence of intergranular polarization from the high temperature data. The data at 800 K (dotted line, Fig. 11 inset) do, indeed, indicate a low frequency permittivity which is about 10 times smaller than that at 500 K, in agreement with the deduction made from the modulus spectrum.

#### **4.3.2 (iii) Comparison of Polycrystalline and Single Crystal Electrical Relaxations in Sodium Beta Alumina.**

Both polycrystalline and single crystal sodium beta alumina have been studied by Ingram and coworkers [48,62] using impedance and modulus spectroscopy. These studies offer an excellent illustration of the fine details which can be seen when the optimum formalisms are used for data analysis.

The modulus spectra of the polycrystalline form [40,58,59], and the single crystal in orientations parallel and perpendicular to the conduction plane [58-62] are reproduced in Fig. 7. The polycrystalline modulus spectrum is, essentially, a weighted sum of the two single crystal spectra. Because of the large difference in conductivity between the two orientations, the two components are fairly well resolved in the polycrystalline spectrum. There is no evidence for an intergranular impedance in the polycrystalline resistivity spectrum.

### 4.3.3. Application of Electric Modulus Spectroscopy to Maxwell-Wagner Interfacial Polarization.

When spheres of a material having a conductivity  $\sigma$ , and relative permittivity  $\epsilon_1$  are suspended in a non-conducting medium having a relative permittivity  $\epsilon_2$ , an interfacial polarization is observed which has a single relaxation time given by

$$\tau_E = \frac{(2 \cdot \epsilon_1 + \epsilon_2) \cdot \epsilon_0}{\sigma}, \quad (111)$$

and a maximum dielectric loss given by

$$\epsilon''_{\max} = \left[ \frac{9 \cdot \phi_f \cdot \epsilon_1^2}{2(2\epsilon_1 + \epsilon_2)} \right] \cdot \left[ 1 + \frac{3 \cdot \phi_f \cdot (\epsilon_2 - \epsilon_1)}{2\epsilon_1 + \epsilon_2} \right] \quad (112)$$

where  $\phi_f$  is the volume fraction of spheres. These equations are valid only if the spheres do not interact electrically with one another. This dielectric loss phenomenon is known as Maxwell-Wagner polarization [4,68].

Like other interfacial effects, Maxwell-Wagner polarization may be viewed as a charge build-up between two parallel  $RC$  elements in series (as described in sections 2.4 and 3.4). Thus, in principle, the single loss peak observed in  $\epsilon''$  should correspond to two peaks in  $M''$  and  $\rho''$  (section 3.4). For the Maxwell-Wagner effect the effective resistance of the suspending medium is infinite, so that only a single peak in  $M''$  and  $\rho''$  reflecting the  $RC$  loss in the sphere should be observed. However, their position and intensities reflect the relaxation of the sphere itself, whereas the dielectric loss also reflects the permittivity of the surrounding medium.

The Maxwell-Wagner effect can be observed in emulsions of water in heptane [68], stabilized by the surfactant sorbitol tristearate. Since water in these emulsions can be supercooled to  $-35^\circ\text{C}$  on a routine basis, the Maxwell-Wagner effect affords an excellent opportunity to measure the permittivity and conductivity of super-cooled water. However, as will be seen the emulsifying agent complicates the situation to such an extent that  $\epsilon''$  is of little value, and useful information can only be gained from the  $M''$  spectra. Because the emulsions studied have a high volume fraction of water (ca. 30%), the modulus will also be seen to circumvent complications due to particle interactions at high concentrations. The method of data analysis presented here should therefore prove to be of general utility in analyzing Maxwell-Wagner type polarizations which cannot be studied by the usual dielectric loss method.

The observed dielectric loss spectra for a 30% water emulsion at a number of temperatures is given in Fig. 12a. It is clear that the maximum loss  $\epsilon''_{\max}$  decreases with decreasing temperature. This is the reverse of what is predicted by eq. (112), since the permittivity  $\epsilon_1$  of water increases with decreasing temperature and  $\epsilon''_{\max}$  is proportional to  $\epsilon_1$ . The latter is derived by observing that for water in heptane  $2\epsilon_1 \gg \epsilon_2$  and

$$\epsilon''_{\max} \approx \left( \frac{9 \cdot \phi_f \cdot \epsilon_1}{4} \right) \cdot \left( 1 - \frac{3 \cdot \phi_f}{2} \right). \quad (113)$$

The modulus spectra are shown in Fig.12b, and their height also decreases with decreasing temperature. However, since  $M''_{\max}$  is proportional to the inverse of the permittivity of the water droplet this trend is in the correct direction, i.e. the permittivity increases with decreasing temperature. By comparing  $M''_{\max}$  at 0°C with the known permittivity of water at that temperature, the proportionality constant is fixed and the permittivity at lower temperatures can be determined. The values of  $\epsilon'$  for water derived from a least squares quadratic fit to 8 data points between 0°C and -35°C are compared with the values derived from the observed permittivity of a dilute suspension of water droplets in a polymeric emulsifier [69], in Table 1. The agreement is well within the  $\pm 2\%$  uncertainties of each method, thus confirming that the modulus formalism is indeed valuable for the analysis of Maxwell-Wagner polarization. If the average permittivity for the modulus derived data is equated to the datum from ref. [69], then the average deviation between the two data sets average is 0.2.

### **Permittivity of Supercooled Water**

Temperature °C	$\epsilon'$ from original modulus analysis	$\epsilon'$ from modified modulus analysis	$\epsilon'$ from (ref. [69])
-5°	89.9	91.1	90.9
-10°	92.1	93.3	93.4
-15°	94.5	95.7	95.6
-20°	97.1	98.4	98.3
-25°	99.8	101.1	100.8
-30°	102.8	104.1	104.2
-35°	105.9	107.3	107.7

#### 4.4. Conductivity and Dielectric Relaxation in the Temperature Domain.

To illustrate the points raised in section XXX2.5, it is desirable that a material exhibit both dielectric and conductivity relaxations. Aqueous electrolyte glasses fulfill this need since they often exhibit dielectric relaxations below the glass transition temperature  $T_g$  and a conductivity relaxation in the vicinity of  $T_g$ . The temperature dependences of  $\epsilon''$ ,  $\epsilon'$ ,  $\tan \delta$ ,  $M''$  and  $\rho''$  taken at 1 Hz for a monomeric hydrate glass are shown in Fig. 13. There are a number of features in these spectra which warrant discussion. First, it is apparent that  $\rho''$  is quite featureless in the temperature domain and contains little information. This is a reflection of  $\ln \omega$  and  $1/T$  not being equivalent variables for this function. For a single relaxation time this can be made explicit:

$$\rho'' = \frac{M'}{e_0 \cdot \omega} = \left( \frac{\tau_D}{e_0 \cdot \epsilon'} \right) \cdot \frac{\omega \cdot \tau_D}{1 + \omega^2 \cdot \tau_D^2} \quad \text{peak in } \omega \text{ domain} \quad (114)$$

$$\rho'' = \frac{M'}{e_0 \cdot \omega} = \left( \frac{1}{e_0 \cdot \omega \cdot \epsilon'} \right) \cdot \frac{\omega^2 \cdot \tau_D^2}{1 + \omega^2 \cdot \tau_D^2} \quad \text{no peak in } \tau \text{ domain} \quad (115)$$

The observed decrease in  $\rho''$  in the vicinity of the conductivity relaxation (where  $\tan \delta \approx 1$  and  $M''$  passes through its high temperature maxima), is due to  $\rho''$  being proportional to  $M'$  at constant frequency [eq. XXX] and the decrease in  $M'$  with decreasing  $1/T$  in the conductivity relaxation region.

Of the remaining loss functions, there is a steady increase in resolution in going from  $\epsilon''$ , to  $\tan \delta (= \epsilon''/\epsilon')$  to  $M'' (\approx \epsilon''/\epsilon'^2)$ . This is probably due to the gradual increase in  $\epsilon'$  offsetting the more or less steady rise in  $\epsilon''$  as the temperature increases.

The resolution of the conductivity and dielectric relaxations improve with decreasing frequency for the data given in Fig. 15. This is usually the case, but exceptions do occur. An example of the latter may be found in data on an ion containing polymer [70], in which the resolution of the dielectric loss from the conductivity background *improves* with increasing frequency. This occurs because the activation energy for conductivity in this case is smaller than that of the dielectric loss, and yet the conductivity relaxation occurs at a higher temperature (lower intrinsic frequency). For the aqueous glass [24] the activation energy for conductivity is higher because the material is ionic and the high activation energy for viscous flow ("structural" relaxation) in the glass transition region is included in the conductivity activation energy.

Masking of a dielectric relaxation by a high background conductivity at all accessible frequencies is often observed. An illustration of the effect in the temperature domain is shown in Fig. 16, where the dielectric relaxation of a glassy aqueous solution of a lithium salt is masked to an increasing extent by the increased conductivity accompanying the substitution of Li ions by protons. A similar effect has been observed by Howell [23], where the dielectric relaxation of glycerol was masked by the conductivity of dissolved lithium chloride.

The effect of activation energy on the relaxation width in the temperature domain is also illustrated in Fig. 16. The modulus spectrum of the pure acid is wider on a  $1/T$  scale than

those of the lithium containing materials, because the activation energy for conductivity is lower for the acid. When the spectra are plotted as a function of  $\langle E_A \rangle / R \cdot T$  in Fig. 16 inset, the (lower frequency) conductivity relaxations are seen to be of comparable widths. It should be noted, however, that the higher frequency secondary relaxations are characterized by lower average activation energies, so that the temperature scale given is not applicable to them. This overlap of temperature scales which are normalized by *different* average activation energies is a major source difficulty in the analysis of relaxations in the temperature domain.

### **Concluding Remarks**

It is apparent from the different applications of the various relaxation formalisms described in section 4 that, generally speaking, the impedance formalisms  $\rho^*$  and  $M^*$  are best suited for the analysis of ac conductivity of conducting electrolytes. For the extrapolation of electrode polarization effects to get data relevant to the bulk electrolyte the complex impedance plane is the most useful method of analysis. For bulk relaxation effects, including those due to intergranular impedances, spectra of  $\rho''$  and  $M''$  together appear to be the most useful. If the bulk relaxation is to be analyzed with minimal interference from interfacial effects, whether these be at the electrode interface, grain boundaries or other sources, the electric loss modulus is unsurpassed. The examples cited emphasize also that a large amount of information which is contained in experimental ac data may be lost if the wrong method of data analysis is employed.

### **Acknowledgements**

The author is indebted to a number of researchers for their help in clarifying many of the concepts discussed here, including Dr. M. D. Ingram, Professor A. Eisenberg, Professor C. T. Moynihan and Professor C. A. Angell.

## Appendix A1

### Summary of Relaxation Formalisms and their Limiting Values.

1. (a) Geometric cell constant  $\equiv k = \ell/A$  for parallel electrodes of area  $A$  separated by  $\ell$
- (b) Geometric capacitance  $\equiv C_0 = \epsilon_0/k$

#### 2. Relationships between Functions

$$M^* \equiv 1/\epsilon^* = i \cdot \epsilon_0 \cdot \omega \cdot \rho^* = i \cdot C_0 \cdot \omega \cdot Z^*$$

$$\rho^* \equiv 1/\sigma^* = 1/(i \cdot \epsilon_0 \cdot \omega \cdot \epsilon^*)$$

$$\sigma^* = i \cdot \epsilon_0 \cdot \omega \cdot \epsilon^*$$

#### 3. Definitions in terms of conductance $G_p$ in parallel with capacitance $C_p$ .

##### (a) Permittivity $\epsilon^*$

$$\epsilon^* = \epsilon' + i \cdot \epsilon''$$

$$\lim_{\omega \rightarrow 0} \epsilon^* = \lim_{\omega \rightarrow 0} \epsilon' = \epsilon_0$$

$$\epsilon' = C_p / C_0$$

$$\lim_{\omega \rightarrow \infty} \epsilon^* = \lim_{\omega \rightarrow \infty} \epsilon' = \epsilon_\infty$$

$$\epsilon'' = G_p / \omega \cdot C_0$$

##### (b) Conductivity $\sigma^*$

$$\sigma^* = \sigma' - i \cdot \sigma''$$

$$\lim_{\omega \rightarrow 0} \sigma' = \sigma_0 = 1/\rho_0$$

$$\sigma' = \epsilon_0 \cdot \omega \cdot \epsilon'' = k \cdot G_p$$

$$\sigma'' = \epsilon_0 \cdot \omega \cdot \epsilon' = k \cdot \omega \cdot C_p$$

##### (c) Electric Modulus $M^*$

$$M^* = M' - i \cdot M''$$

$$\lim_{\omega \rightarrow 0} M' = 0$$

conductivity relaxation

$$M' = \frac{\epsilon'}{\epsilon'^2 + \epsilon''^2} = \left( \frac{C_0}{C_p} \right) \cdot \frac{\omega^2 \cdot R_p^2 \cdot C_p^2}{1 + \omega^2 \cdot R_p^2 \cdot C_p^2} = \frac{\epsilon'}{1 + (\tan \delta)^2}$$

$$\lim_{\omega \rightarrow 0} M' = \frac{1}{\epsilon_0}$$

dielectric relaxation

$$M'' = \frac{\epsilon''}{\epsilon'^2 + \epsilon''^2} = \left( \frac{C_0}{C_p} \right) \cdot \frac{\omega \cdot R_p \cdot C_p}{1 + \omega^2 \cdot R_p^2 \cdot C_p^2} = \frac{\epsilon'' \cdot \tan \delta}{1 + (\tan \delta)^2}$$

$$\lim_{\omega \rightarrow \infty} M' = \frac{1}{\epsilon_\infty}$$

conductivity relaxation

(d) Resistivity  $\rho^*$

$$\rho^* = \rho' + i \cdot \rho''$$

$$\lim_{\omega \rightarrow 0} \rho^* = \lim_{\omega \rightarrow 0} \rho' = 1 / \sigma_0$$

$$\rho' = \frac{k \cdot G_p}{1 + \omega^2 \cdot R_p^2 \cdot C_p^2} = \frac{\epsilon_0 \cdot \omega \cdot \epsilon''}{1 + (\tan \delta)^2}$$

$$\rho'' = \left( \frac{k \cdot \omega \cdot C_p}{1 + \omega^2 \cdot R_p^2 \cdot C_p^2} \right) = \frac{\epsilon_0 \cdot \omega \cdot \epsilon'}{1 + (\tan \delta)^2}$$

(e) Loss tangent

$$\tan \delta = \frac{\epsilon''}{\epsilon'} = \frac{M''}{M'} = \frac{\sigma'}{\sigma''} = \frac{\rho'}{\rho''} = \frac{1}{\omega \cdot R_p \cdot C_p}$$

4. Definitions in terms of resistance  $R_s$  in series with capacitance  $C_s$ .

(a) Permittivity  $\epsilon^*$

(f) Conductivity  $\sigma^*$

(g) Electric Modulus  $M^*$

(h) Resistivity  $\rho^*$

(i) Loss tangent

$$\tan \delta = \frac{\epsilon''}{\epsilon'} = \frac{M''}{M'} = \frac{\sigma'}{\sigma''} = \frac{\rho'}{\rho''} = \frac{1}{\omega \cdot R_p \cdot C_p}$$

## Appendix A2 Specific Distribution Functions

There are a large number of distribution functions which have been used to describe experimental dielectric loss data, and some of the more common ones used for conductivity relaxations are summarized here. The functions are defined, where possible, in terms of  $M^*(i \cdot \omega)$ ,  $\phi(t)$  or  $(d\phi/dt)$ , and  $g(\ln \tau)$ . The moments of  $g(\ln \tau)$  are also given, where possible. Relations giving the parameters of the functions in terms of features of the corresponding loss spectrum (imaginary component as a function of frequency) are also given. The spectrum features are defined in Figure A2-1.

When fitting a distribution function for  $\epsilon^*$  to a function such as  $M^*$ , it should be recognized that their real components differ. For normalized functions, in which the dispersion in the real component is unity, the relations are

### A2-1 Davidson-Cole Function

1.

$$M^* = \frac{M_\infty}{1 - (1 - i \cdot \omega \cdot \tau_0)^{-\gamma}};$$

$$M' = M_\infty \cdot \left[ 1 - (\cos \phi)^\gamma \cdot (\cos \gamma \phi) \right];$$

$$M'' = M_\infty \cdot \left[ 1 - (\cos \phi)^\gamma \cdot (\sin \gamma \phi) \right];$$

$$\phi \equiv \arctan(\omega \cdot \tau_0);$$

$$0 < \gamma \leq 1$$

2.

$$-\frac{d\phi}{dt} = \left( \frac{1}{\tau_0 \cdot \Gamma(\gamma)} \right) \cdot \left( \frac{t}{\tau_0} \right)^{\gamma-1} \cdot \exp\left(-\frac{t}{\tau_0}\right), \text{ where } \Gamma \text{ is the gamma function.}$$

3.

$$g(\ln \tau) = \begin{cases} \left( \frac{1}{\pi} \right) \cdot \sin(\gamma \cdot \pi) \cdot \left[ \frac{\tau}{(\tau_0 - \tau)} \right] & \tau < \tau_0 \\ = 0 & \tau \geq \tau_0 \end{cases}$$

4.

$$\begin{aligned}\langle \tau^n \rangle &= \tau_0^n \cdot \left[ \frac{\Gamma(n+\gamma) \cdot \Gamma(1-\gamma)}{\Gamma(n+1)} \right] \cdot \frac{\sin(\gamma \cdot \pi)}{\pi} \\ &= \frac{\tau_0^n}{n} \cdot \left[ \frac{\Gamma(n+\gamma)}{\Gamma(n) \cdot \Gamma(\lambda)} \right] \\ &= \frac{\tau_0^n}{n} \cdot \left[ \frac{1}{B(n, \gamma)} \right]\end{aligned}$$

where  $B(n, \gamma)$  is the beta function.

Special cases:

$$\langle \tau \rangle = \gamma \cdot \tau_0; \quad \langle \tau^2 \rangle = \left( \frac{\tau_0^2}{2} \right) \gamma \cdot (1+\gamma)$$

5.

$$\gamma^{-1} \approx -1.2067 + 1.6715 \cdot \Delta + 0.222569 \cdot \Delta^2 \quad 1.14 \leq \Delta \leq 0.31 \quad 0.15 \leq \gamma \leq 1.00$$

Gives  $\gamma$  to  $\pm 0.002$  for  $\gamma \leq 0.9$ , too high by 0.007 at  $\gamma = 1.0$ 

6.

$$(a) \quad M_{\max}'' = M_{\infty}'' \cdot (\cos \phi_{\max})^{\gamma} \cdot \sin(\gamma \cdot \phi_{\max}) \quad \text{where } \phi_{\max} = \frac{\pi}{2 \cdot (1+\gamma)}$$

$$(b) \quad M_{\max}'' = M_{\infty}'' \cdot \left[ \sin \left( \frac{\gamma \cdot \pi}{2 \cdot (1+\gamma)} \right) \right]^{1+\gamma}$$

$$(c) \quad M_{\max}'' = M_{\infty}'' \cdot (0.07571 + 0.68277 \cdot \gamma - 0.26176 \cdot \gamma^2)$$

Gives  $M_{\max}''$  to  $\pm 0.003$  ( $< 2\%$ ) for  $0.2 \leq \gamma \leq 1.0$ 

7.

$$\tau_0 = \frac{\tan \phi_{\max}}{\omega_{\max}}$$

8.

$$\log_{10} \tau_0 \approx -0.9276 + \frac{0.76486}{\gamma} - \frac{0.056511}{\gamma^2} - \log_{10} (f_{1/2}^+)$$

where  $f_{1/2}^+$  is the upper frequency at which  $M'' = M_{\max}''/2$ Gives  $\log_{10} \tau_0$  to  $\pm 0.01$

9.

$$\log_{10} \tau_0 \approx -1.586 + \frac{0.25915}{\gamma} - \frac{0.035695}{\gamma^2} - \log_{10} (f_{1/2}^-)$$

where  $f_{1/2}^-$  is the lower frequency at which  $M'' = M''_{\max}/2$

Same accuracy as (8) above.

## A2-2. Williams-Watts

The first physical application of this function appears to be a statistical theory of rupture by Wibull [73-75] and the time derivative is referred to as the Weibull distribution function in some statistics compilations. Its application to mechanical relaxation phenomena in inorganic glasses has been reviewed by Douglas [77], and its application to dielectric relaxation was initiated by Williams and Watts [14,72]

1.

$$\begin{aligned} \phi(t) &= \exp \left[ - \left( \frac{t}{\tau_0} \right)^\beta \right]; \\ -\frac{d\phi(t)}{dt} &= \left( \frac{\beta}{t} \right) \cdot \left( \frac{t}{\tau_0} \right)^\beta \cdot \exp \left[ - \left( \frac{t}{\tau_0} \right)^\beta \right]; \\ &= \left( \frac{\beta}{\tau_0} \right) \cdot \left( \frac{t}{\tau_0} \right)^{\beta-1} \cdot \exp \left[ - \left( \frac{t}{\tau_0} \right)^\beta \right] \quad 0 \leq \beta \leq 1 \end{aligned}$$

2.

$$\begin{aligned} M^*(i \cdot \omega) &= M_\infty \cdot \sum_1^\infty (-1)^{n-1} \cdot \left( \frac{\Gamma(n \cdot \beta + 1)}{\Gamma(n + 1)} \right) \cdot (i \cdot \omega \cdot \tau_0)^{-n \cdot \beta} \\ &= M_\infty \cdot \sum_1^\infty (-1)^{n-1} \cdot (\omega \cdot \tau_0)^{-n \cdot \beta} \cdot \left( \frac{\Gamma(n \cdot \beta + 1)}{\Gamma(n + 1)} \right) \cdot \left[ \cos \left( \frac{n \cdot \pi \cdot \beta}{2} \right) + i \cdot \sin \left( \frac{n \cdot \pi \cdot \beta}{2} \right) \right] \end{aligned}$$

$$\beta = 0.5 [3a]:$$

$$3. \text{ For } \frac{M^*(z)}{M_\infty} = \frac{1 - \pi^{1/2} \cdot (1+i)}{\xi} \cdot \exp(-z^2) \cdot \operatorname{erfc}(i \cdot z),$$

where  $\xi = (8 \cdot \omega \cdot \tau_0)^{1/2}$ ,  $z = \frac{(1-i)}{\xi}$ , and  $\operatorname{erfc}$  is the complementary error function. The function

$$M^* M_5 [1 - i^2 (1-j) p^{-1} \exp(-Z^2) \operatorname{erfc}(-jz)]$$

where  $p = (8wr_0) z (1+j)p$  and  $\text{erfc}$  is the complementary error function. The function  $\exp(-z^2) \cdot \text{erfc}(i \cdot z)$  is frequently tabulated and included in software packages.

#### 4. Hamon Approximation

$$\frac{M''(\omega)}{M_\infty} = \beta \cdot \left(\frac{\pi}{5}\right)^{\beta-1} \cdot \left(\frac{1}{\omega \cdot \tau_0}\right)^\beta \cdot \exp\left[-\left(\frac{\pi}{5 \cdot \omega \cdot \tau_0}\right)^\beta\right] \quad \omega \cdot \tau_0 > 1$$

Approximation improves as  $\beta$  decreases and  $\omega \cdot \tau_0$  increases.

#### 5.

$$\begin{aligned} \langle \tau^n \rangle &= \left(\frac{\tau_0^n}{\beta}\right) \cdot \Gamma\left(\frac{n}{\beta}\right) & n \geq 1 \\ &= \left(\frac{\tau_0^n}{n}\right) \cdot \Gamma\left(1 + \frac{n}{\beta}\right) \end{aligned} \quad \langle T_n \rangle = (T_0 f, \sim) r(n/\sim)$$

#### 6.

$$\beta^{-1} \approx -0.08984 + 0.96479 \cdot \Delta - 0.004604 \cdot \Delta^2$$

Gives  $\beta$  to  $\pm 0.001$  for  $\beta \leq 0.7$  and to within  $\pm 0.002$  for  $\beta \geq 0.95$

#### 7.

$$\frac{M''_{\max}}{M_\infty} = -0.0065 + 0.61368 \cdot \beta - 0.10561 \cdot \beta^2$$

Gives  $M''_{\max} / M_\infty$  to within  $\pm 0.001$  for  $0.3 \leq \beta \leq 1$

#### 8.

$$\log_{10} \tau_0 \approx -1.001 + 0.40882 \cdot \beta^2 - 0.2048 \cdot \beta^4 - \log_{10} f_{\max}$$

Since this paper was written, Lindsay and Patterson [*J. Chem. Phys.* **73** 3348 (1980)], published the expression

$$\log_{10} (\omega \cdot \tau_0)_{\max} \approx -0.2307 + 0.386425 \cdot \beta^2 - 0.16086 \cdot \beta^4, \text{ corresponding to}$$

$$\log_{10} \tau_0 \approx -1.029 + 0.40882 \cdot \beta^2 - 0.2048 \cdot \beta^4 - \log_{10} f_{\max}.$$

#### 9.

$$\log_{10} \tau_0 \approx -0.8621 + 0.527137 \cdot \beta^2 - 0.0144123048 \cdot \beta^4 - \log_{10} f_{1/2}^-$$

#### 10.

$$\log_{10} \tau_0 \approx -0.7675 + 0.50924 \cdot \beta^2 - 0.019872 \cdot \beta^4 - \log_{10} f_{1/2}^+$$

## A2-3. Cole-Cole Function [47]

1.

$$\frac{M^*}{M_\infty}(\alpha) = \left\{ 1 - \frac{1}{\left[ 1 + (i \cdot \omega \cdot \tau_0)^{1-\alpha} \right]} \right\};$$

$$\frac{M'}{M_\infty}(\alpha) = \left( \frac{1}{2} \right) \left\{ 1 + \frac{\sin\left(\frac{\alpha \cdot \pi}{2}\right)}{\left[ \cosh(\theta) + \sin\left(\frac{\alpha \cdot \pi_0}{2}\right) \right]} \right\};$$

$$\frac{M''}{M_\infty}(\alpha) = \left( \frac{1}{2} \right) \left\{ \frac{\cos\left(\frac{\alpha \cdot \pi}{2}\right)}{\left[ \cosh(\theta) + \sin\left(\frac{\alpha \cdot \pi_0}{2}\right) \right]} \right\};$$

$$\frac{M'''}{M_\infty}(\alpha) = \cos\left(\frac{\alpha \cdot \pi}{2}\right) \cdot \left[ (\omega \cdot \tau_0)^{1-\alpha} + (\omega \cdot \tau_0)^{-(1-\alpha)} + 2 \cdot \sin\left(\frac{\alpha \cdot \pi}{2}\right) \right]$$

where  $\theta \equiv (1-\alpha) \cdot \ln(\omega \cdot \tau_0)$ 

2.

$$g(\ln \tau) = \left( \frac{1}{\pi} \right) \cdot \left( \frac{\tau_0}{\tau} \right)^{1-\alpha} \cdot \frac{\sin(\alpha \cdot \pi)}{1 - 2 \cdot \left( \frac{\tau_0}{\tau} \right)^{1-\alpha} \cdot \cos(\alpha \cdot \pi) + \left( \frac{\tau_0}{\tau} \right)^{2(1-\alpha)}}$$

3.

$$-\left( \frac{d\phi}{dt} \right) = \left[ \frac{\alpha}{\tau_0 \cdot \Gamma(1+\alpha)} \right] \cdot \left( \frac{t}{\tau_0} \right)^{-(1-\alpha)} \quad (t/\tau_0) \ll 1$$

$$= \left[ \frac{\alpha}{\tau_0 \cdot \Gamma(1+\alpha)} \right] \cdot \left( \frac{t}{\tau_0} \right)^{-(1+\alpha)} \quad (t/\tau_0) \gg 1$$

4.

$$\frac{M''_{\max}}{M_\infty} = \sec\left(\frac{\alpha \cdot \pi}{2}\right) - \tan\left(\frac{\alpha \cdot \pi}{2}\right)$$

5.

$$\tau_0 = \left( \frac{1}{\omega_{\max}} \right)$$

6.

$$\frac{1}{1-\alpha} \approx 0.242106 + 0.648435 \cdot \Delta + 0.0098624 \cdot \Delta^2$$

Gives  $\alpha$  to  $\pm 0.002$   
 $0 \leq \alpha \leq 0.70 < cz < 0.700$

#### A2-4. Resistivity Function from Davidson-Cole Electric Modulus

The parameters  $M_\infty$ ,  $\tau_0$ ,  $\gamma$  refer to the Davidson-Cole modulus function.

1.

$$\rho'' = \frac{\rho_0 \left[ 1 - (\cos \phi)^\gamma \cdot \cos(\gamma \cdot \phi) \right]}{\gamma \cdot \omega \cdot \tau_0}$$

where  $\rho_0 = \frac{M_\infty \cdot \gamma \cdot \tau_0}{e_0} = \frac{1}{\sigma_0} = \frac{M_\infty \cdot \langle \tau \rangle}{e_0}$  and  $\phi \equiv \arctan(\omega \cdot \tau_0)$

2.

$$\gamma^2 \approx 49.84439 - 75.526329 \cdot \Delta + 28.691692 \cdot \Delta^2$$

where  $\gamma$  is the Davidson-Cole modulus function and  $\Delta$  is the width at half-height (in decades of frequency) of the  $\rho''$  the p" spectrum. Gives  $\gamma$  to  $\pm 0.007$  for  
 $0.4 \leq \gamma \leq 1.0$ ;  $1.144 \leq \Delta \leq 1.287$

3.

$$\log_{10}(\tau_0) \approx -0.5076 - 0.387125 \cdot \gamma + 0.097606 \cdot \gamma^2 - \log_{10}(f_{\max})$$

Gives  $\log_{10}(\tau_0)$  to  $\pm 0.001$   $0.1 \leq \gamma \leq 1.0$

$f_{\max}$  refers to the  $\rho''$  spectrum;  $\tau_0$  and  $\gamma$  to the Davidson-Cole  $M''$  spectrum.

4.

$$\rho''_{\max} \approx \rho_0 \cdot (0.40396 + 0.13135 \cdot \gamma - 0.03568 \cdot \gamma^2)$$

Gives  $\rho''_{\max}$  to  $\pm 0.0003$   $0.1 \leq \gamma \leq 1.0$

5.

$$\alpha(\rho''_{CC}) \approx 0.1699 - 0.238106 \cdot \gamma + 0.068424 \cdot \gamma^2$$

This relates  $\alpha$  for the Cole-Cole resistivity function having the same half width as the

resistivity function derived from a Davidson-Cole modulus function with shape parameter  $\gamma$ .

Gives  $\alpha$

to  $\pm 0.002$  for  $0.1 \leq \gamma \leq 1.0$ .

6.

A comparison of a Cole-Cole  $\rho''$  spectrum with that derived from a Davidson-Cole  $M''$  spectrum is given in Fig. A2.2. The two are seen to be very similar, despite the large asymmetry of the Davidson-Cole function ( $\gamma = 0.2$ )

## FIGURE CAPTIONS

**Figure 1** Equivalent circuit for a Debye-Pellat dielectric relaxation.  $G_0$  is the zero frequency conductance, and  $C_0 \cdot \epsilon_\infty$ , the high frequency limiting capacitance. The relaxation behavior is simulated by the series conductance and capacitance in the lowest arm of the circuit.  $\tau_E$  is the dielectric relaxation time.

**Figure 2** Spectra of the four basic relaxation functions for a representative equivalent circuit.  $\omega$  is the angular frequency in  $\text{radian sec}^{-1}$ . Single primed symbols refer to real components, and double primed symbols to the imaginary components.

(A) Equivalent circuit.

(B) Spectra of the components of the complex conductivity  $\sigma^*$ . The high and low frequency relaxation limits of the real component are shown ( $\sigma_\infty$  and  $\sigma_0$  respectively). The spectrum of  $\sigma''$  with its high frequency limit (proportional to  $\omega$ ) subtracted is also shown.

(C) Spectra of the components of the complex relative permittivity  $\epsilon^*$ . The spectrum of  $\epsilon''$  with the zero frequency conductivity contribution,  $\sigma_0/(e_0 \cdot \omega)$ , subtracted out is also shown. Note the logarithmic scale for  $\epsilon^*$  at low frequencies, and linear scale at high frequencies.

(D) Spectra of the components of the complex resistivity  $\rho^*$ . Logarithmic scales are given in the insets to indicate the presence of the high frequency peak in  $\rho''$  at low frequencies.

(E) Spectra of the components of the complex electric modulus,  $M^*$ . The non-zero low frequency limit of  $M'$  is shown at left.

**Figure 3:** Complex plane plots for the circuit and spectra of Figure 2.

(A) Complex conductivity plane. The low frequency relaxation due to  $C_s$  is shown in the inset (note different scale).

(B) Complex relative permittivity plane. Note the different scales for the low frequency (upper) and high frequency (lower) relaxations.

(C) Complex resistivity plane. Note different scales for each part.

(D) Complex modulus plane.

**Figure 4** Arrhenius plot for conductivity at different fixed measuring frequencies. The dotted line gives the expected high temperature behavior (not measured). Data are for  $\text{Li}_4\text{GeO}_4$  (Ref. 57).

**Figure 5** Complex admittance plane behavior of polycrystalline Ytria-Zirconia solid electrolytes, after Bauerle (Ref. 37).

- (A) Equivalent circuit used in data processing.
- (B) Complex admittance plane for circuit given in (A). The relations between the complex plane parameters and the circuit elements are given at bottom of figure.
- (C) Experimental complex admittance plane behavior. Each relaxation conforms to the Cole-Cole function (see Appendix A2-3). The angles  $\theta$  measure the displacement of semicircle centers below real axis and are related to the width parameter  $\alpha = \theta/90^\circ$ . Four terminal (4T) and direct current (dc) data are indicated. The upper figures refer to measuring frequency in Hz.

**Figure 6** Relaxation functions for the proton conducting glass  $\text{HZnCl}_3 \cdot 4\text{H}_2\text{O}$  at  $-105^\circ\text{C}$  (Ref. 45).

- (A) Spectra of the specific conductivity  $\sigma'$ , relative permittivity  $\epsilon'$  and electric loss modulus  $M''$ . Circles are data points, and solid lines are for the best fit Davidson-Cole function for  $M''$ . Davidson-Cole parameters (see Appendix A2-1) are  $M_\infty = 0.105$ ,  $\gamma = 0.33$ ,  $\tau_0 = 1.07 \times 10^{-3}$  sec.
- (B) Resistivity spectrum. Solid line is spectrum derived from Davidson-Cole function for  $M''$ . Dotted line and circles are observed data points.
- (C) Complex resistivity plane plot. The solid semicircle is that calculated from the Davidson-Cole function for  $M''$ . The low frequency polarization extrapolation is also shown.

**Figure 7** Spectra for single crystal and polycrystalline  $\beta$ -alumina (after Ingram et al, Refs. 48, 60-62) at  $-160^\circ\text{C}$ .

- (A) Electric loss modulus spectra for single crystal in orientations parallel and perpendicular to conduction plane.
- (B) Dielectric loss spectra for single crystal in same orientations as (A).
- (C) Electric loss modulus and impedance spectra for single crystal. Open circles are  $M''$  parallel to conduction planes, closed circles are  $M''$  in perpendicular orientation, and dotted line is  $Z''$  in parallel orientation.
- (D) Electric loss modulus and impedance spectra for polycrystalline  $\beta$ -alumina (Ref. 48,) Note the coincidence of two resolvable modulus peaks with two orientations of single crystal spectra in (A).

**Figure 8** Complex impedance plane data for 2 sintered  $\beta$ -alumina preparations at room temperature (after Armstrong et al, Ref. 20).

(A) Sinter 1 (see Ref. 20 for preparation details).

(B) Sinter 2, with different surface preparations. Note that high frequency extrapolations give self-consistent values for  $\sigma_0$ .

**Figure 9** Complex impedance plane data for  $\text{KHF}_2$  (after Bruinink Ref. 54).

(A) Single crystal  $\alpha$ - $\text{KHF}_2$ , in an atm of  $\text{H}_2$ .

(B) Single crystal of  $\text{KHF}_2$ , in vacuo. Inset gives low frequency relaxation due to electrode polarization.

(C) Polycrystalline  $\beta$ - $\text{KHF}_2$ .

**Figure 10** Relaxation spectra for a cracked and annealed polycrystalline preparation (after Hodge et al, Ref. 41).

(A) Impedance and modulus spectra for the indicated equivalent circuit.

(B) Modulus spectra of cracked (1), partially annealed (2), and fully annealed (3) material.

(C) Impedance spectra corresponding to data given in (B). Note the disappearance of the low frequency relaxation with annealing. The dotted lines are a resolution assuming the low frequency relaxation to be symmetric.

(D) Conductivity spectra corresponding to data given in (B) and (C). Note the great loss of information compared with the spectra given in (C).

**Figure 11** Relaxation spectra for polycrystalline zinc oxide in 1 atm  $\text{O}_2$ . (after Seitz and Sokoly, Ref. 58). Note logarithmic ordinate scales. Circles are data points at 500 K. Dotted line in inset is permittivity spectrum at 800 K.

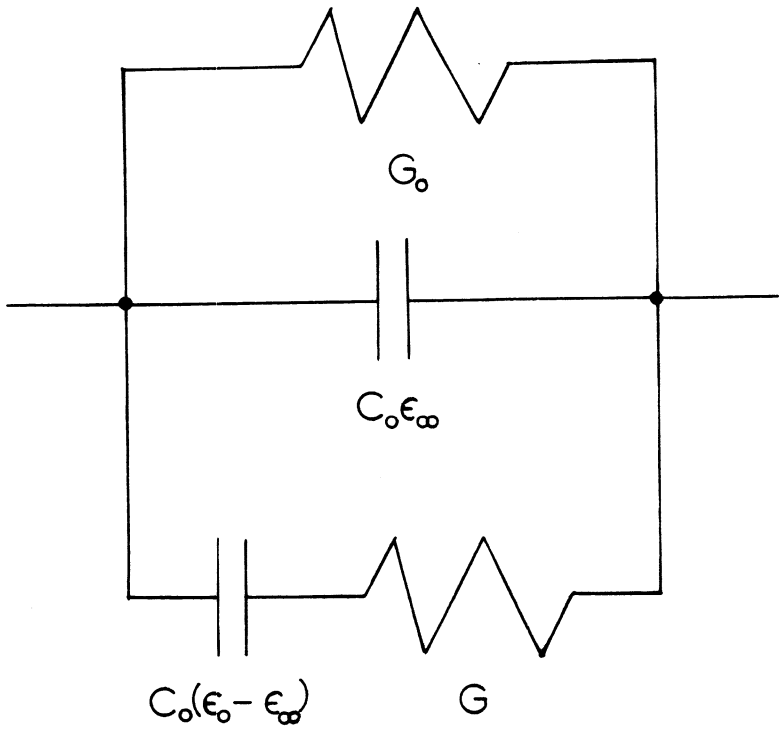
**Figure 12** Temperature dependences of dielectric loss spectra (A) and electric loss modulus spectra (B) of a water in heptane- $\text{CCl}_4$  emulsion (after Hodge and Angell, Ref. 69). Open and closed circles and open and closed squares are data at  $0^\circ$ ,  $-9.8$ ,  $-21.4$  and  $-35.0^\circ\text{C}$ , respectively.

**Figure 13** Relaxation functions in the temperature domain for  $\text{Ca}(\text{NO}_3)_2$  at 1 Hz (from data given by Hodge and Angell, Ref. 24).

**Figure 14** Electric loss moduli versus reciprocal temperature for a series of glassy Li salt/acid mixtures, illustrating masking of the secondary relaxation in Li salt by high conductivity of acid (Ref. 45). Inset: The same data as a function of  $E_A/R \cdot T$ , where  $E_A$  is the average activation energy for the (high temperature) conductivity relaxation.  $\Delta$  denotes shifts of spectra to make conductivity relaxation coincide.

**Figure A2-1** Definition of electric loss modulus parameters.

**Figure A2-2** Comparison of Cole-Cole resistivity spectrum (closed circles) with spectrum derived from Davidson-Cole  $M'$  spectrum (open circles). Note two frequency scale corresponding to shifts made to make half height points coincide. The Cole-Cole function has been normalized to make  $\rho_{\max}''$  coincide with that of Davidson-Cole function.



$$\tau = C_0(\epsilon_0 - \epsilon_\infty)/G$$

Fig 1

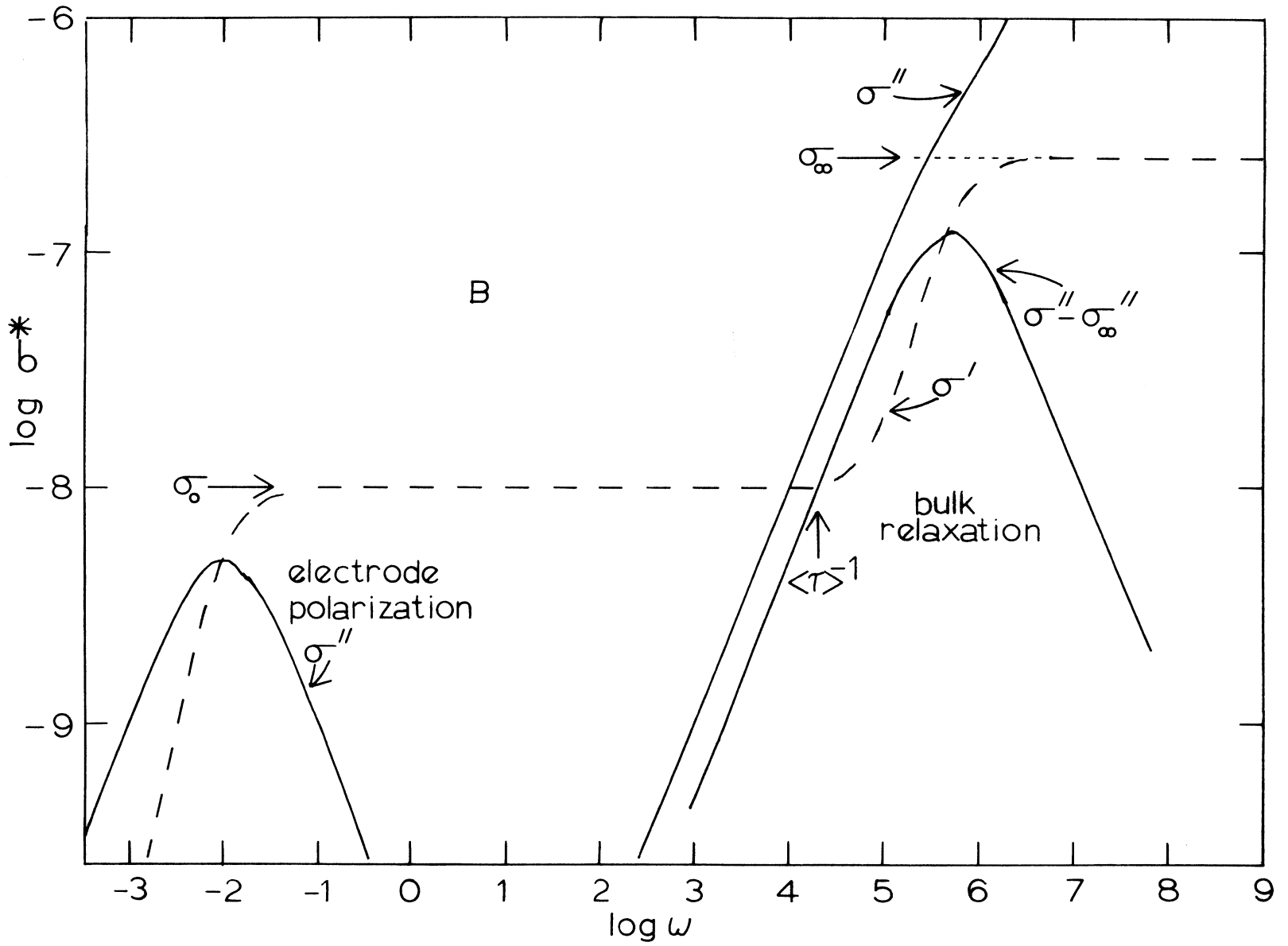


Fig 2B

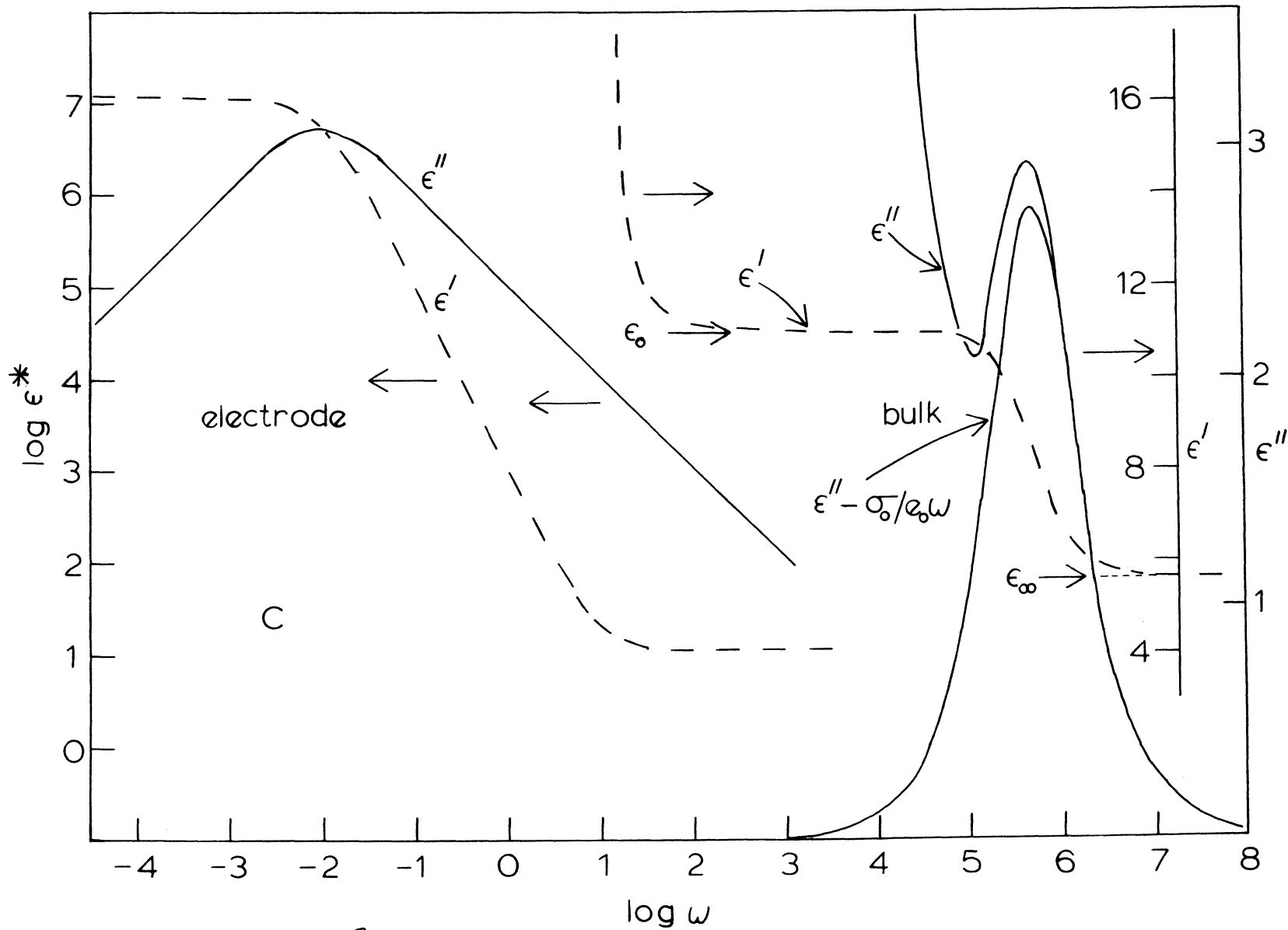


Fig 2c

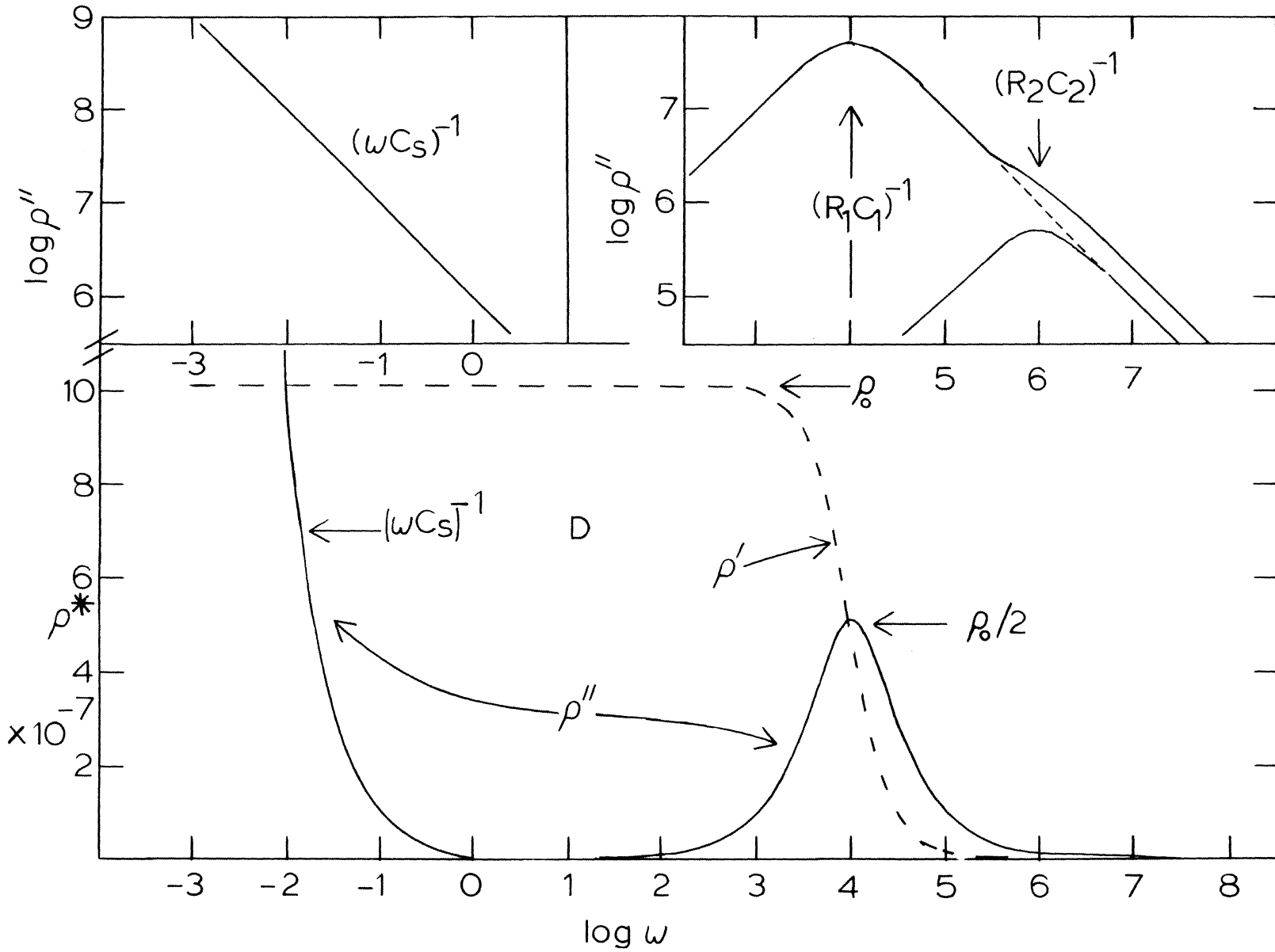


Fig 2D

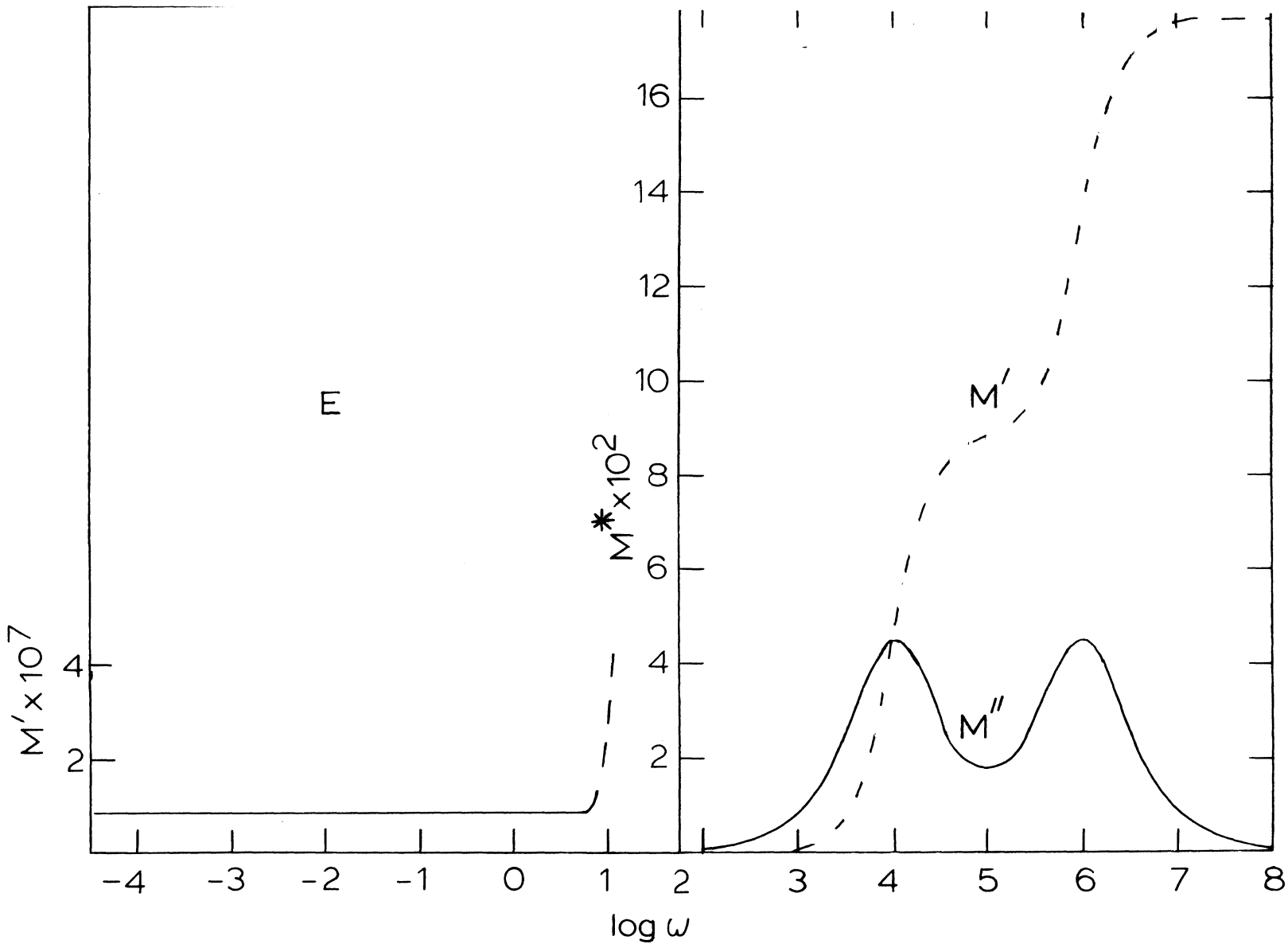
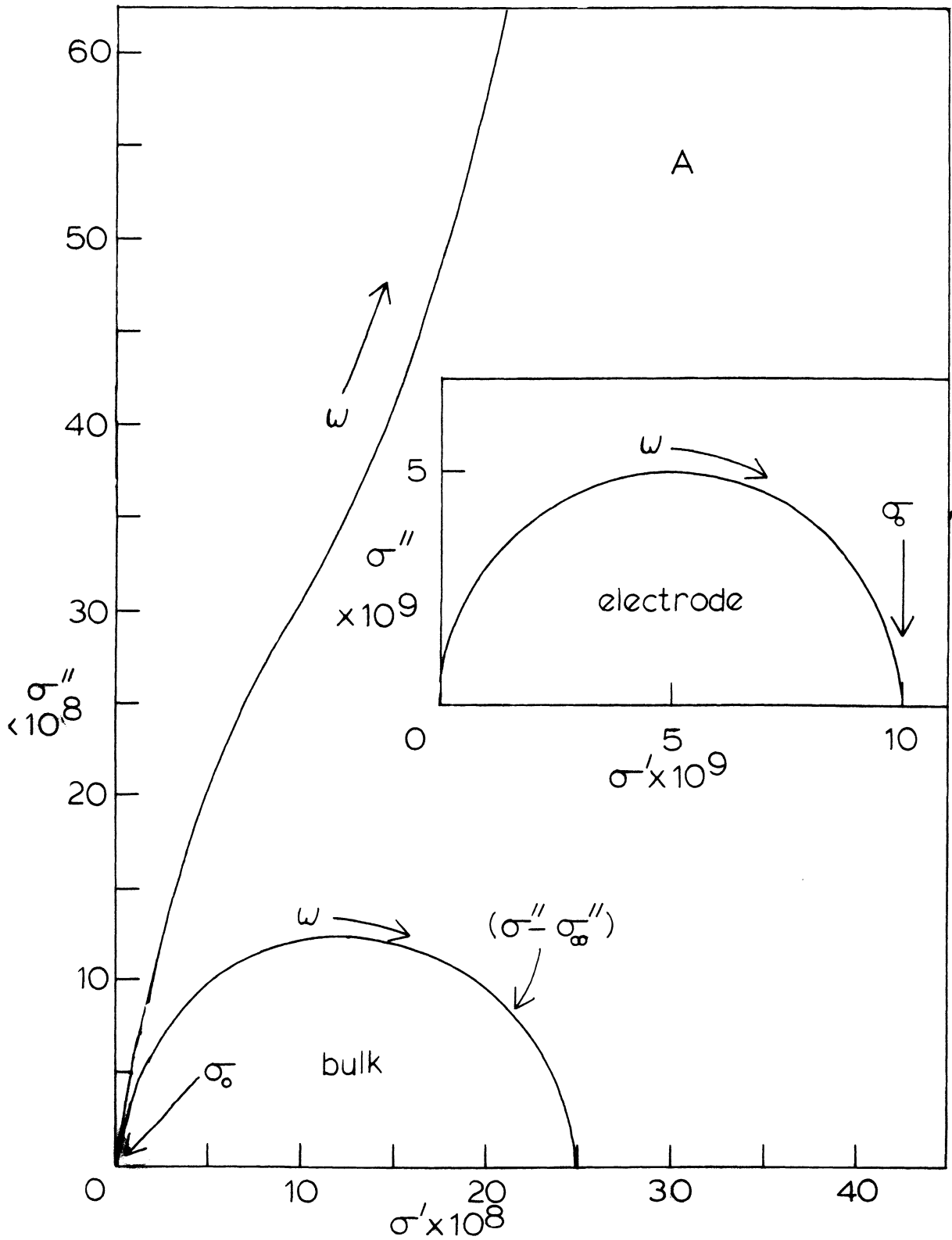


Fig 2E

Fig 3A



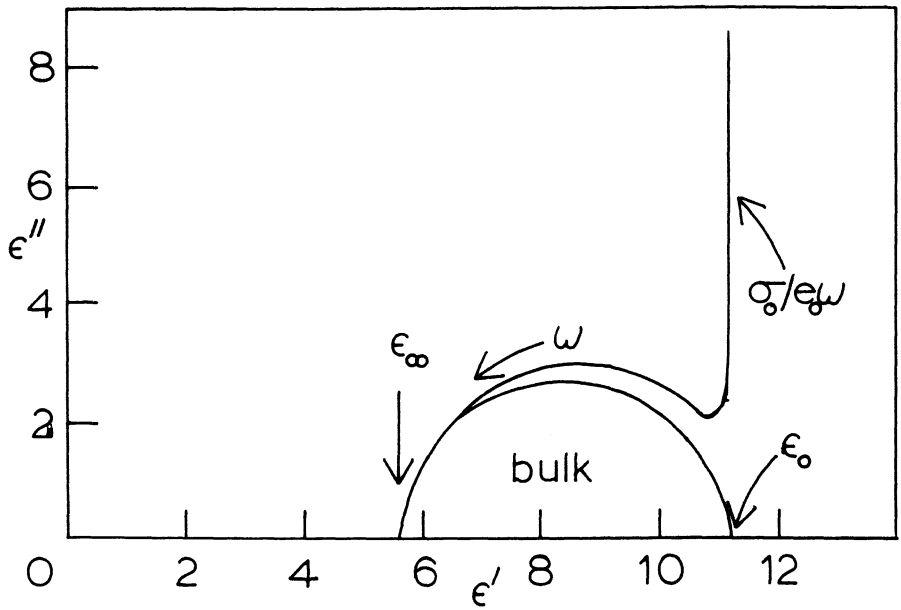
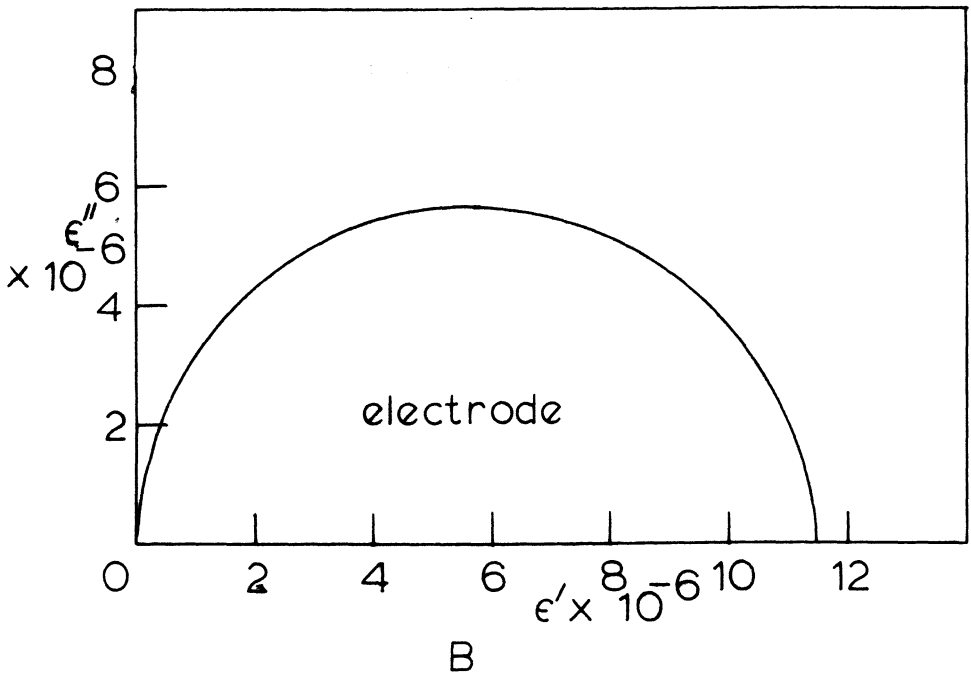


Fig 3B

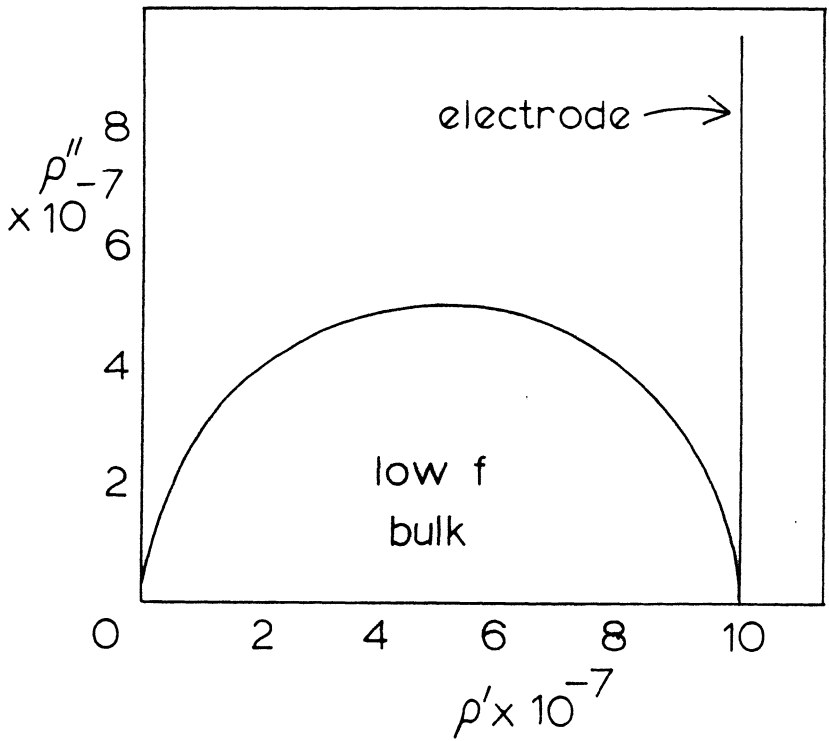
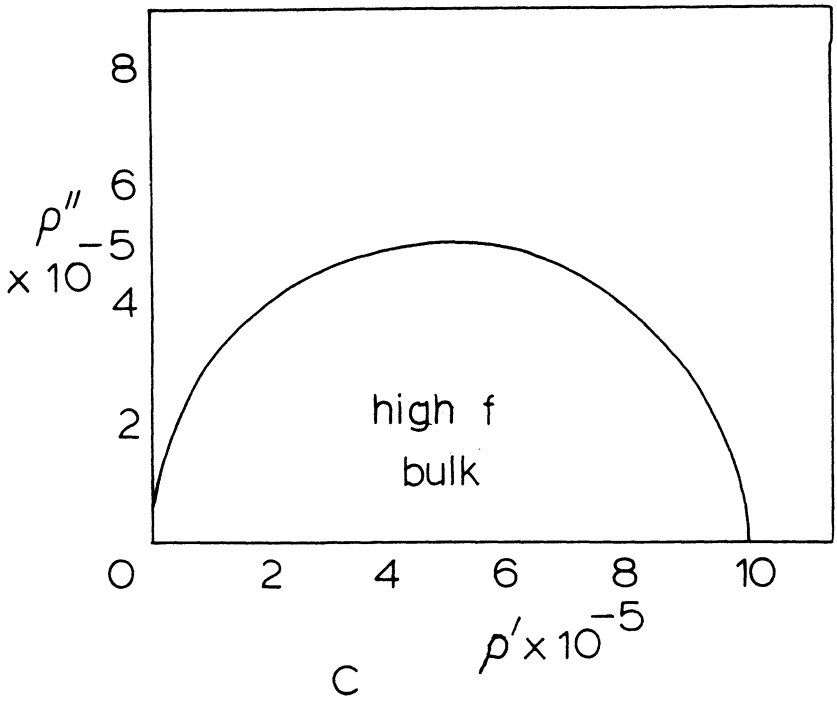


Fig 3C

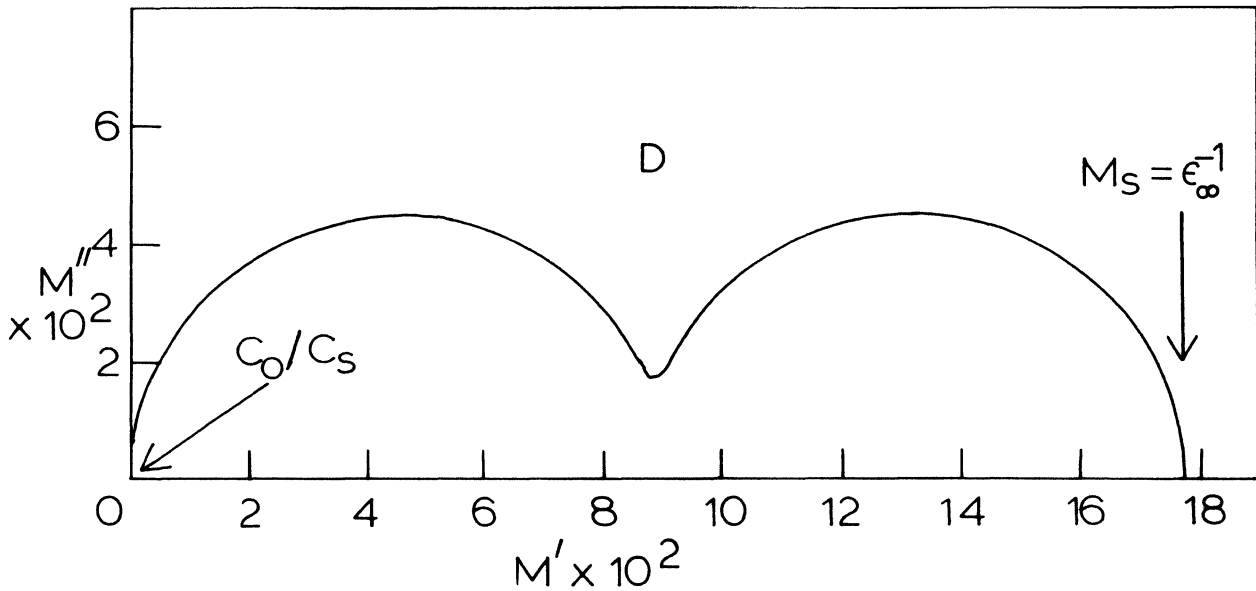
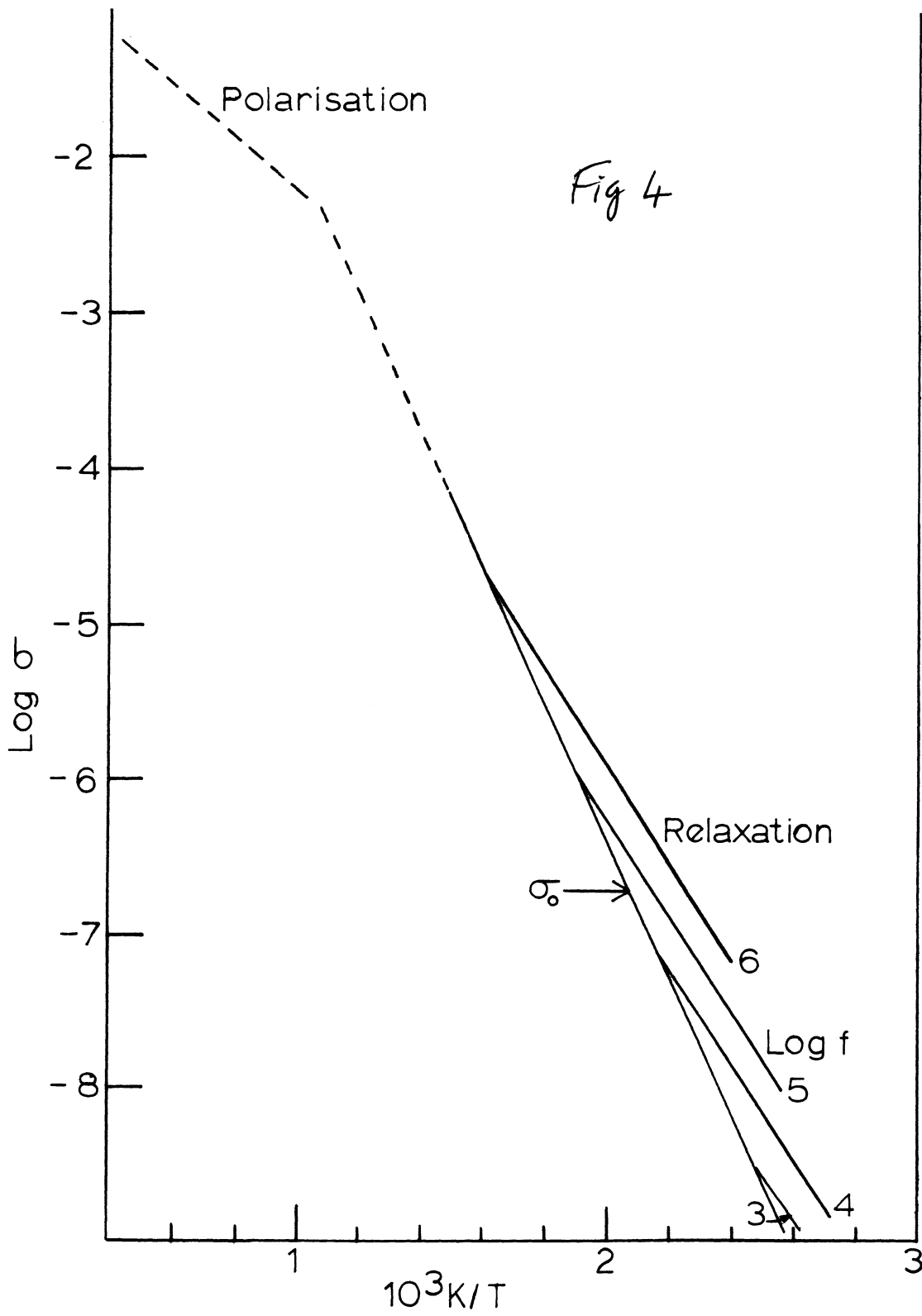
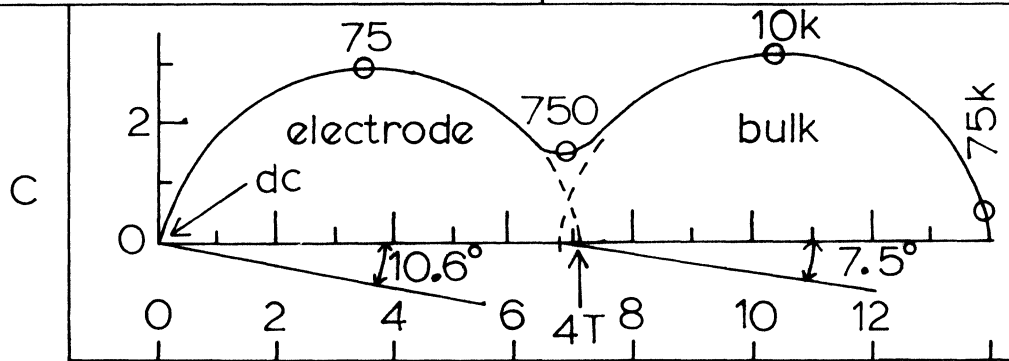
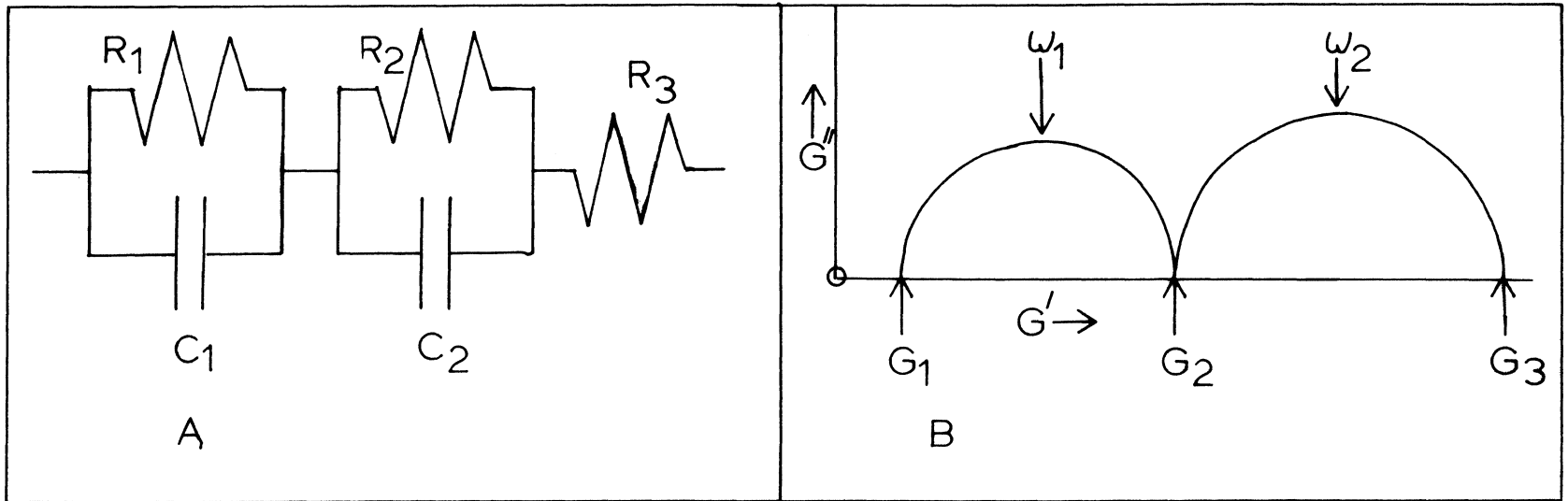


Fig 3D





$$R_1 = G^{-1} + G^{-1}$$

$$R_2 = G^{-1} + G^{-1}$$

$$R_3 = G^{-1}$$

$$C_1 = G_2^2 \left[ w_1 (G_2 - G_1) \right]^{-1}$$

$$C_2 = G_3^2 \left[ w_2 (G_3 - G_2) \right]^{-1}$$

Fig 5

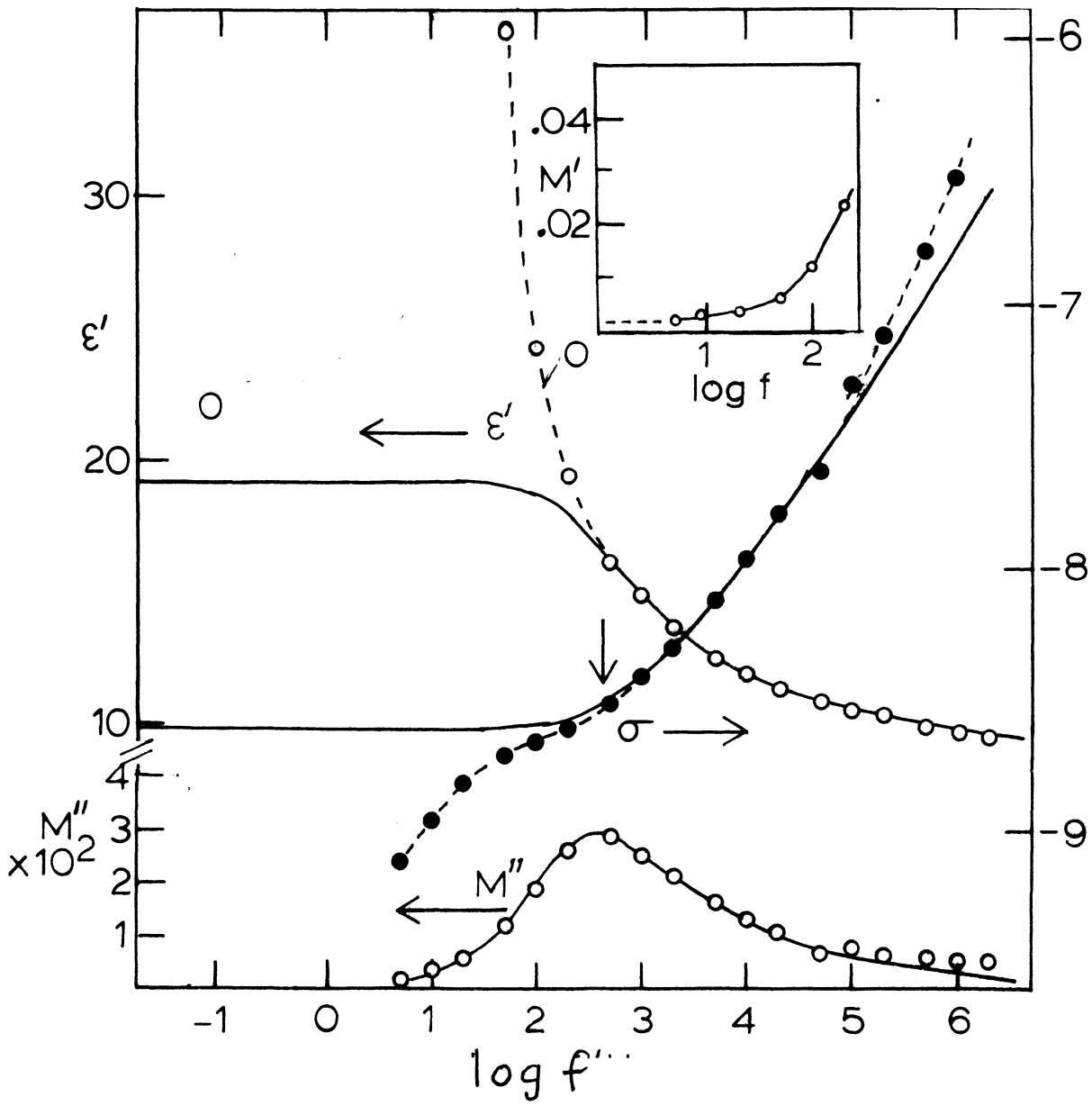


Fig 6A

Fig 6b

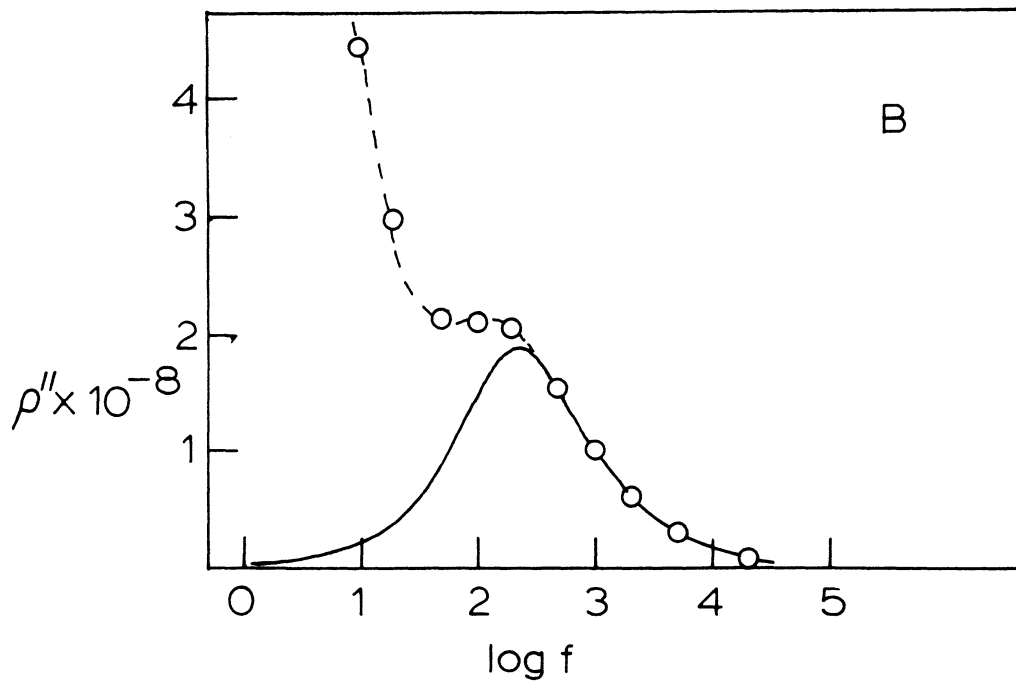
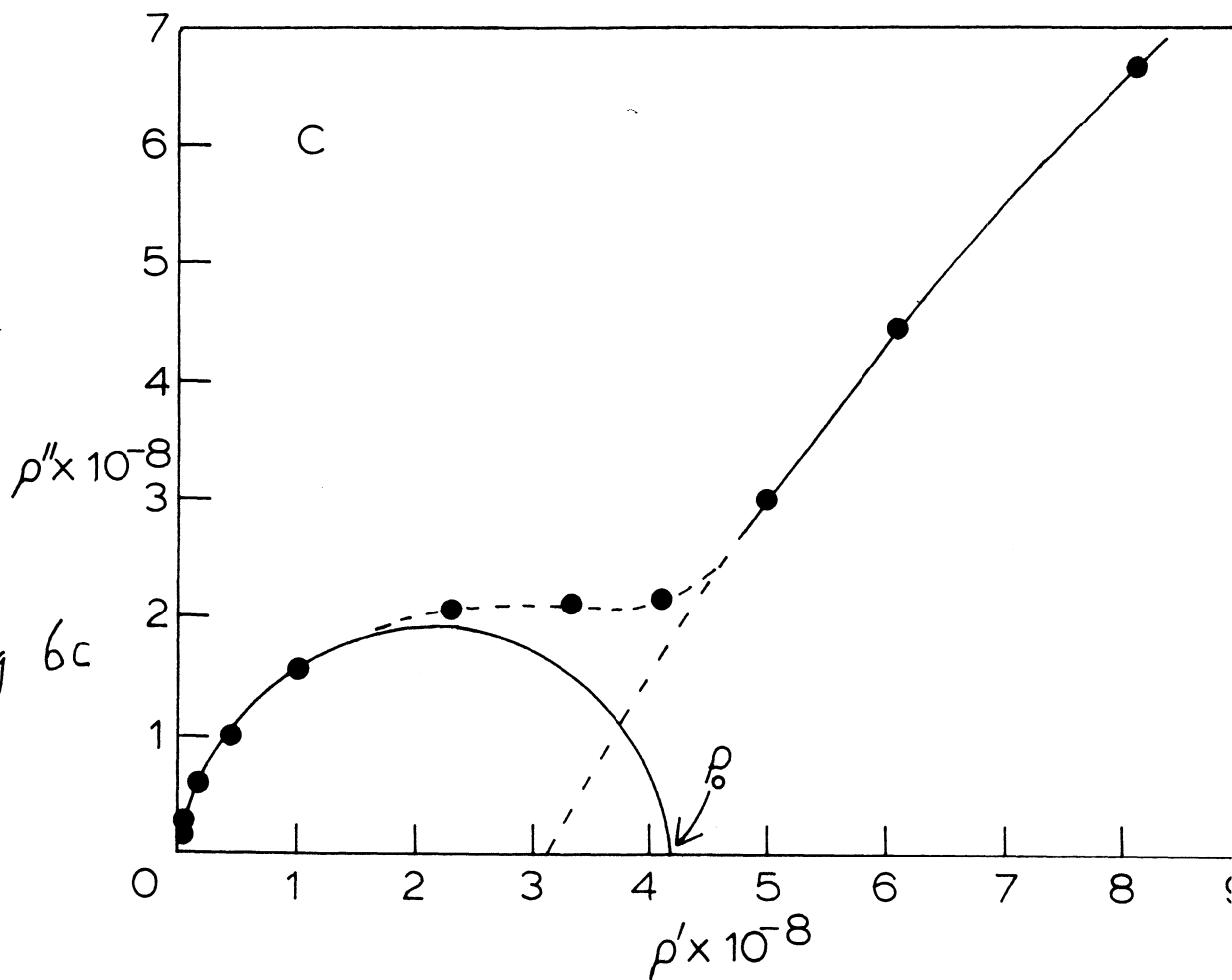


Fig 6c



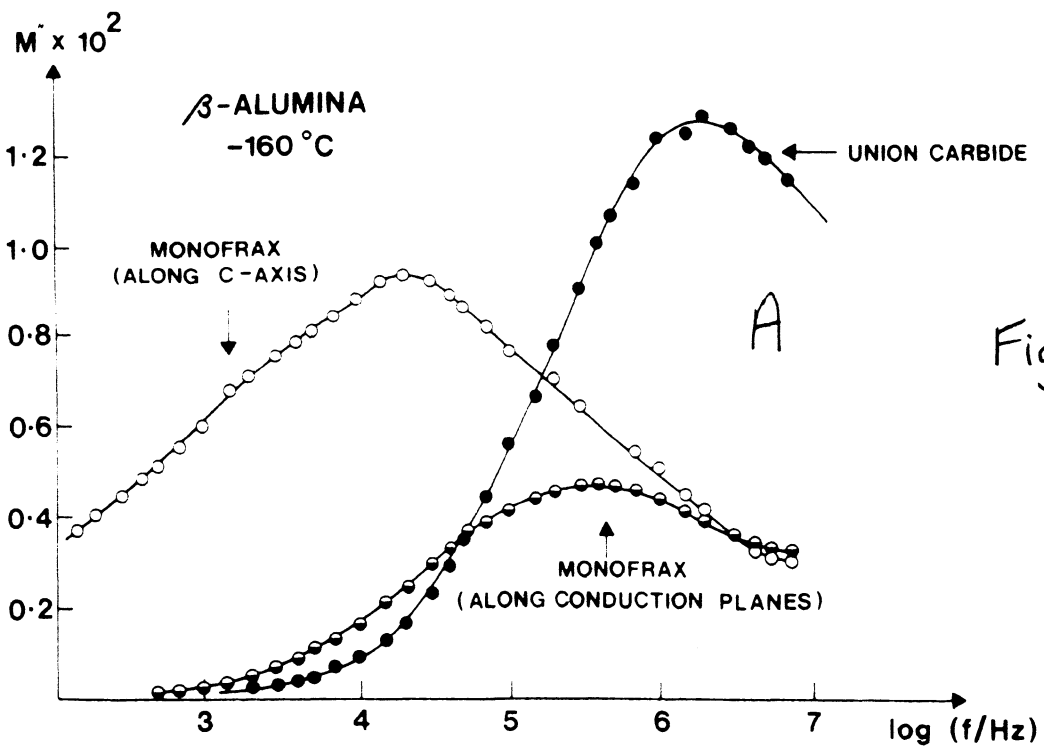
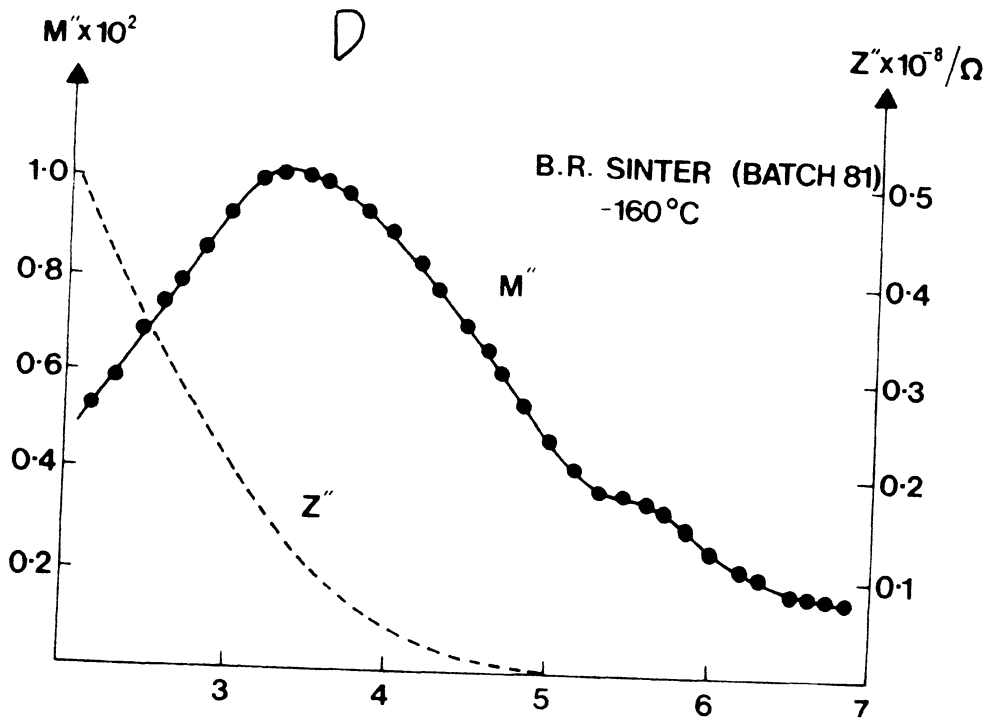
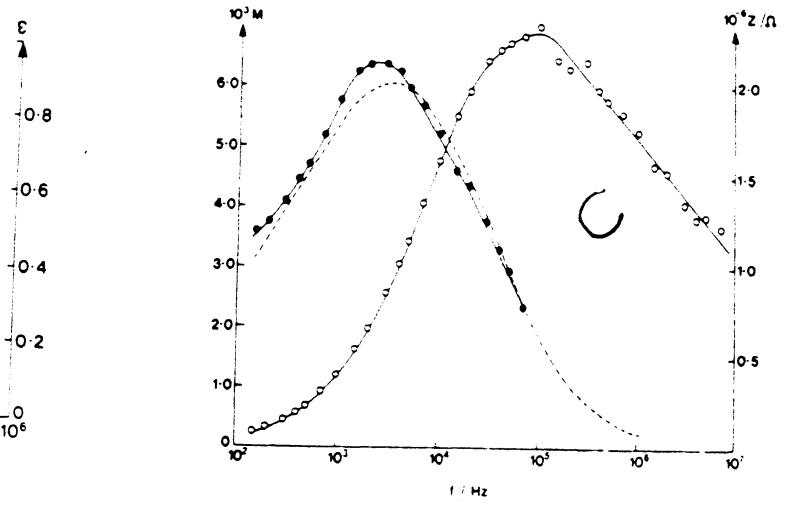
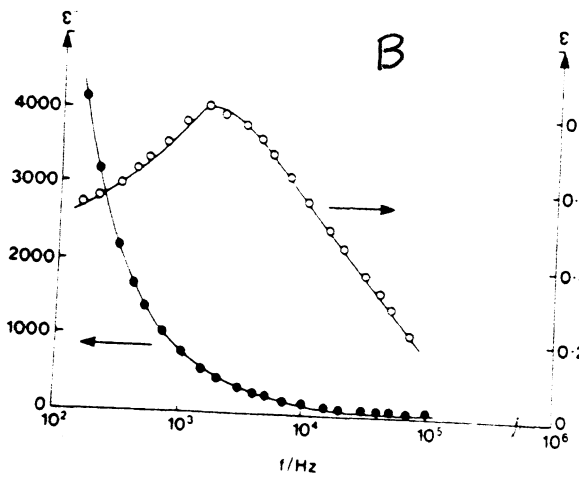


Fig 7



A

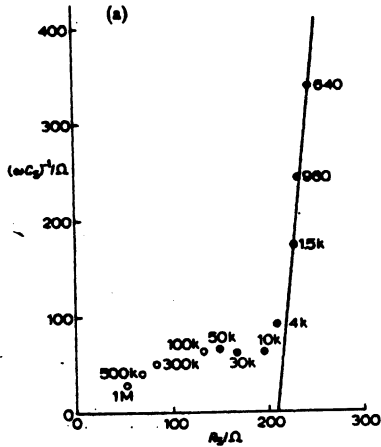


Fig. 8. The impedance of  $\beta'$ -alumina sinter 1. (a) At room temperature

B

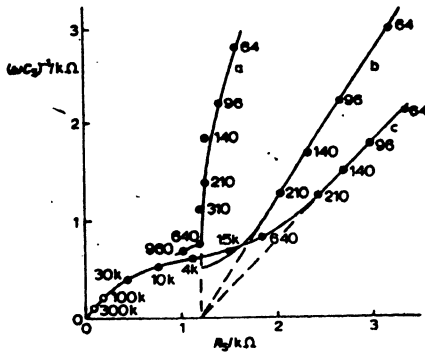
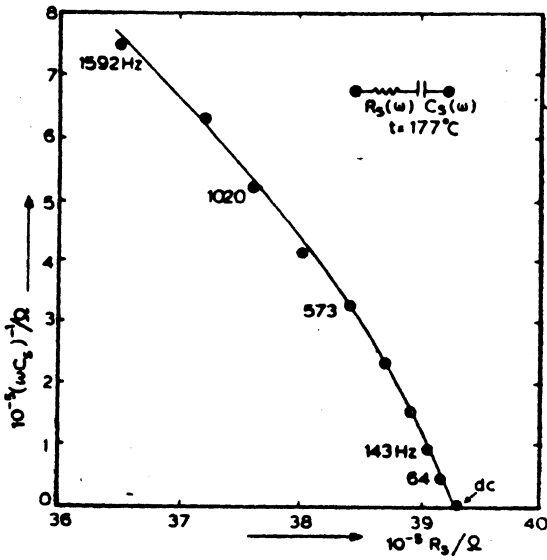
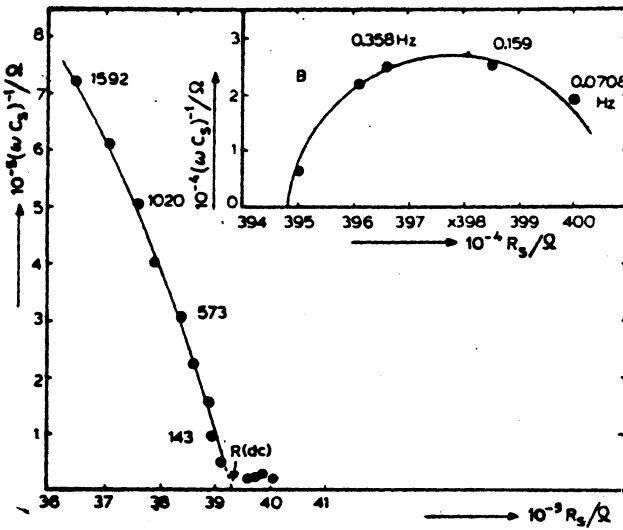


Fig. 9. The impedance of  $\beta'$ -alumina sinter 2 at room temperature showing the effect of different surface preparations.

Fig 8

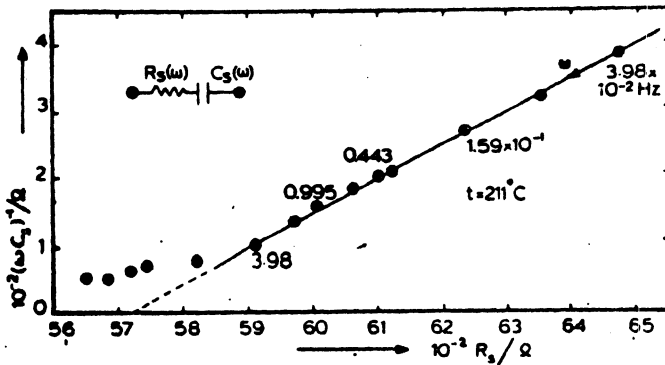


A



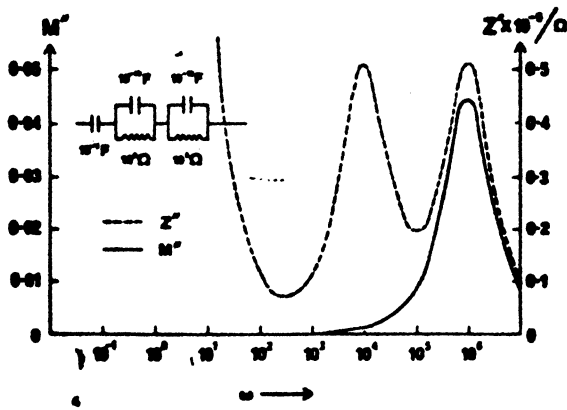
B

Fig 9

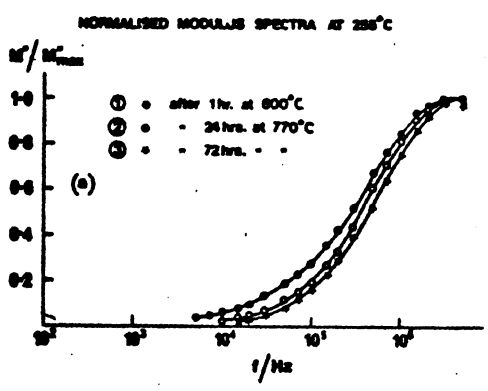


C

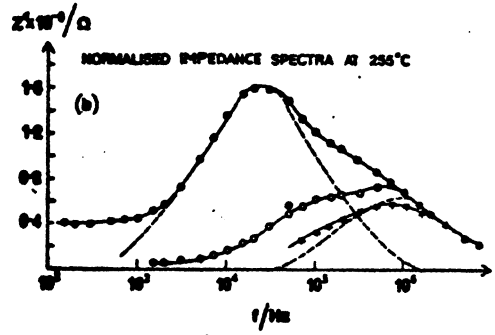
A



B



C



D

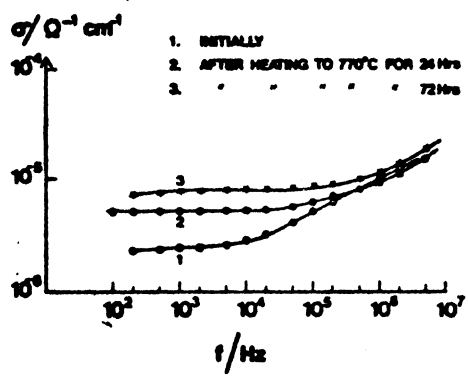


Fig 10

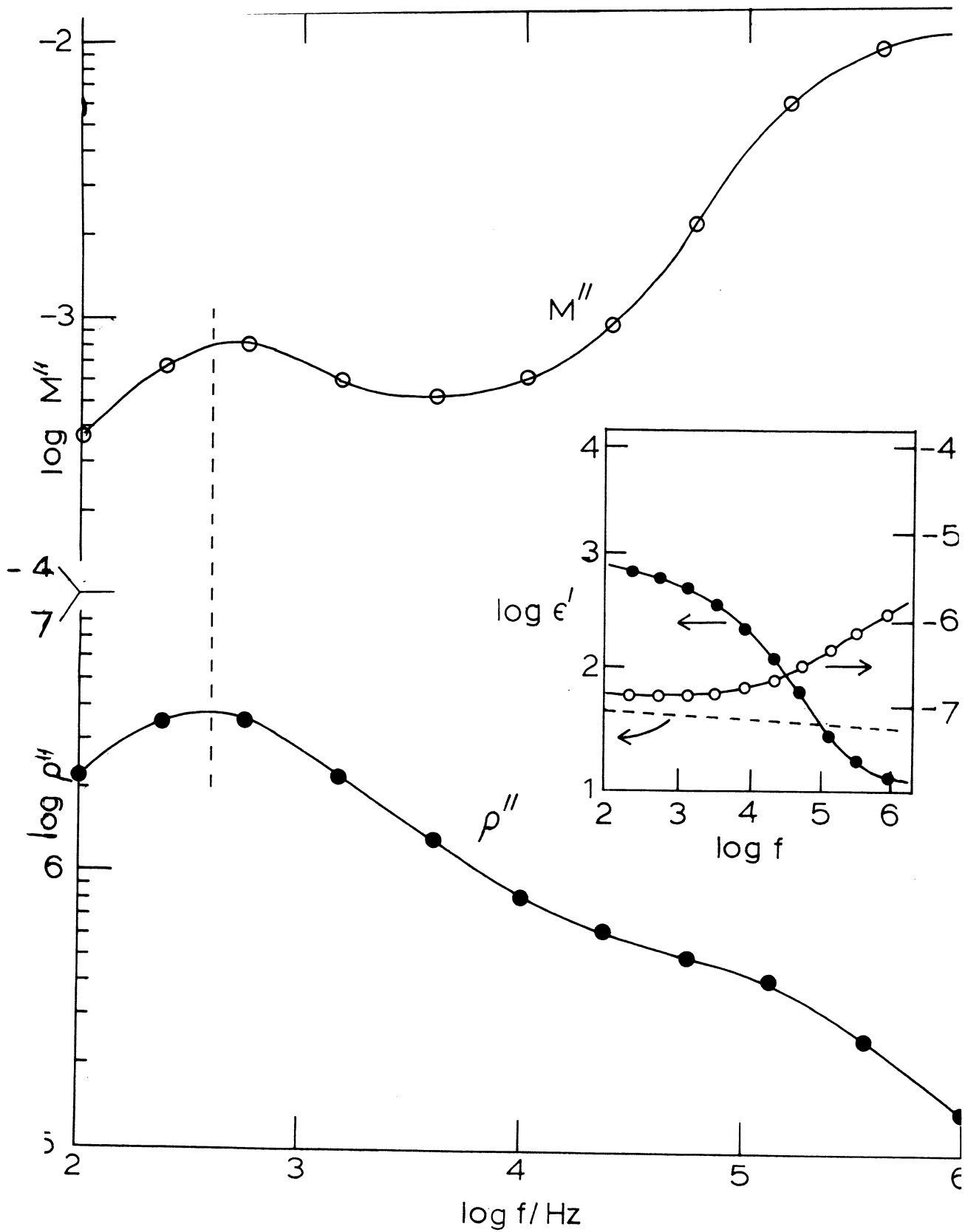


Fig 11

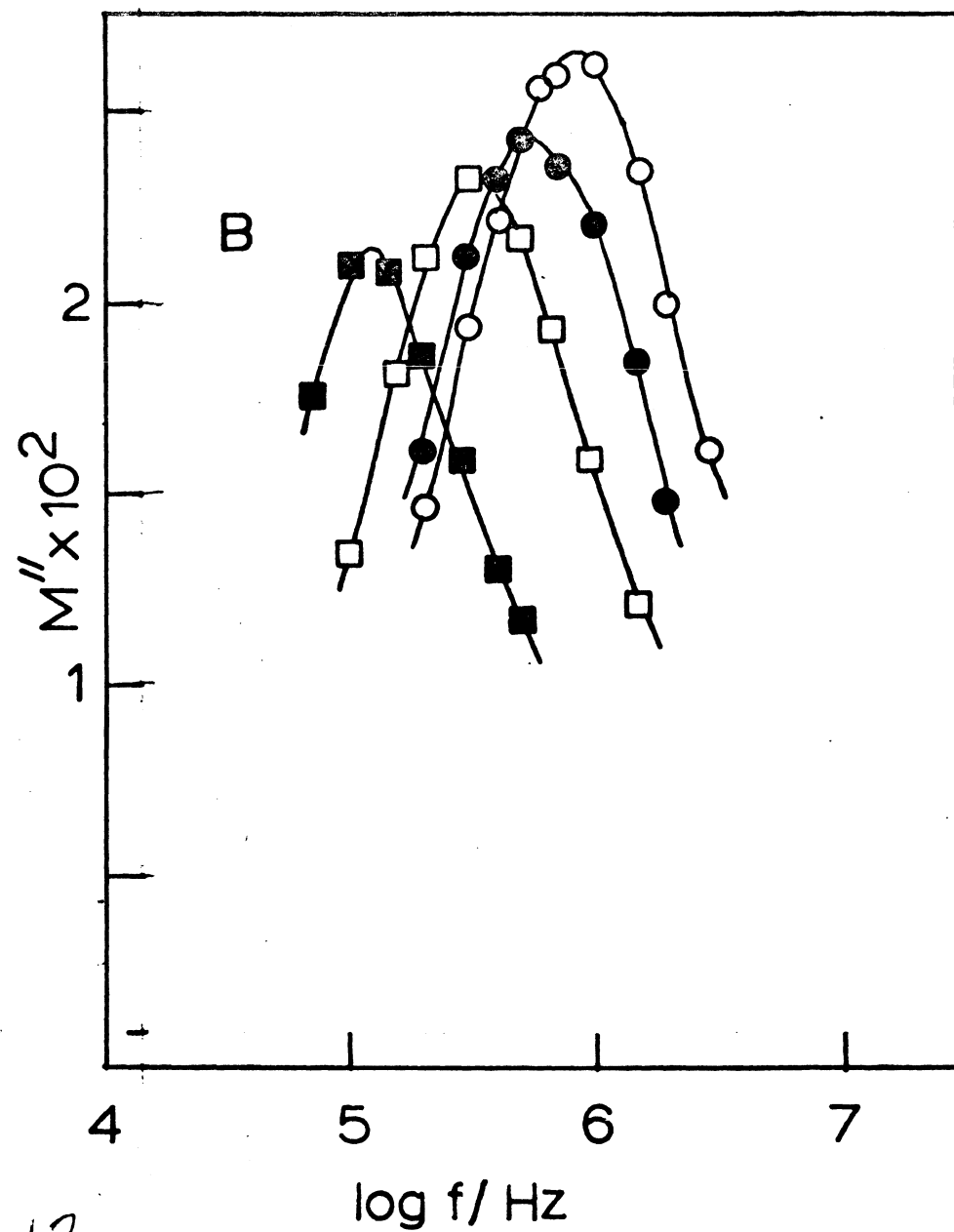
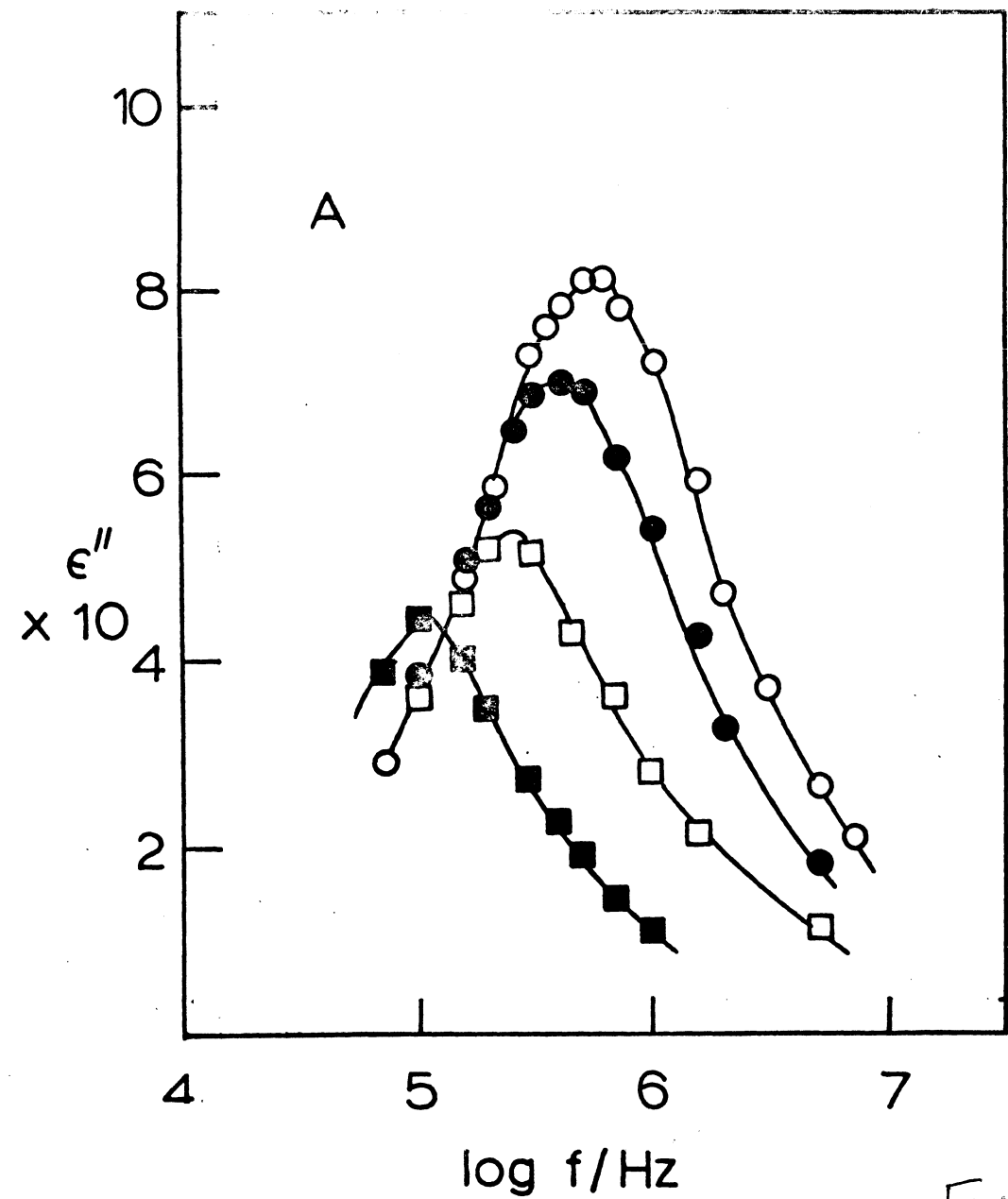
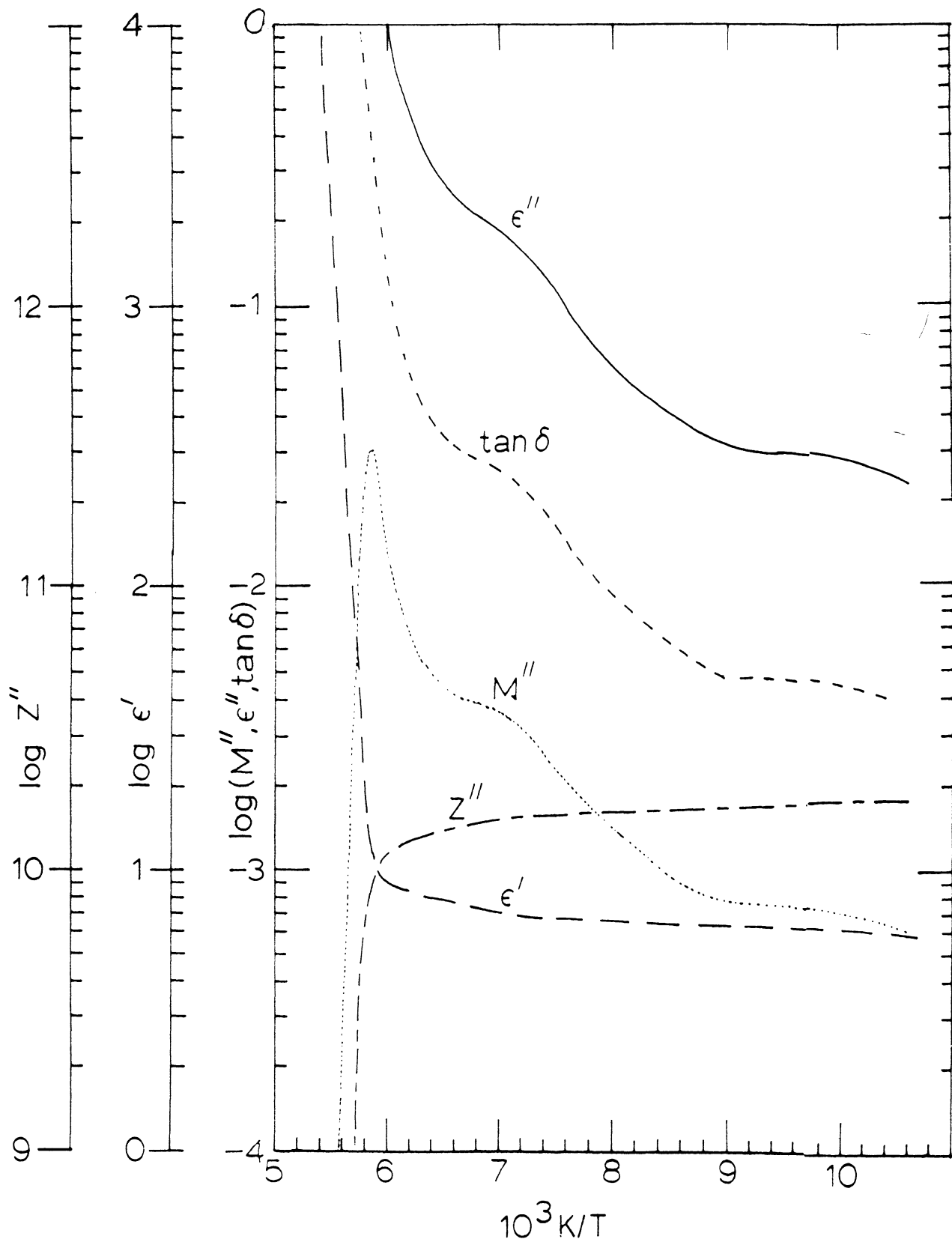
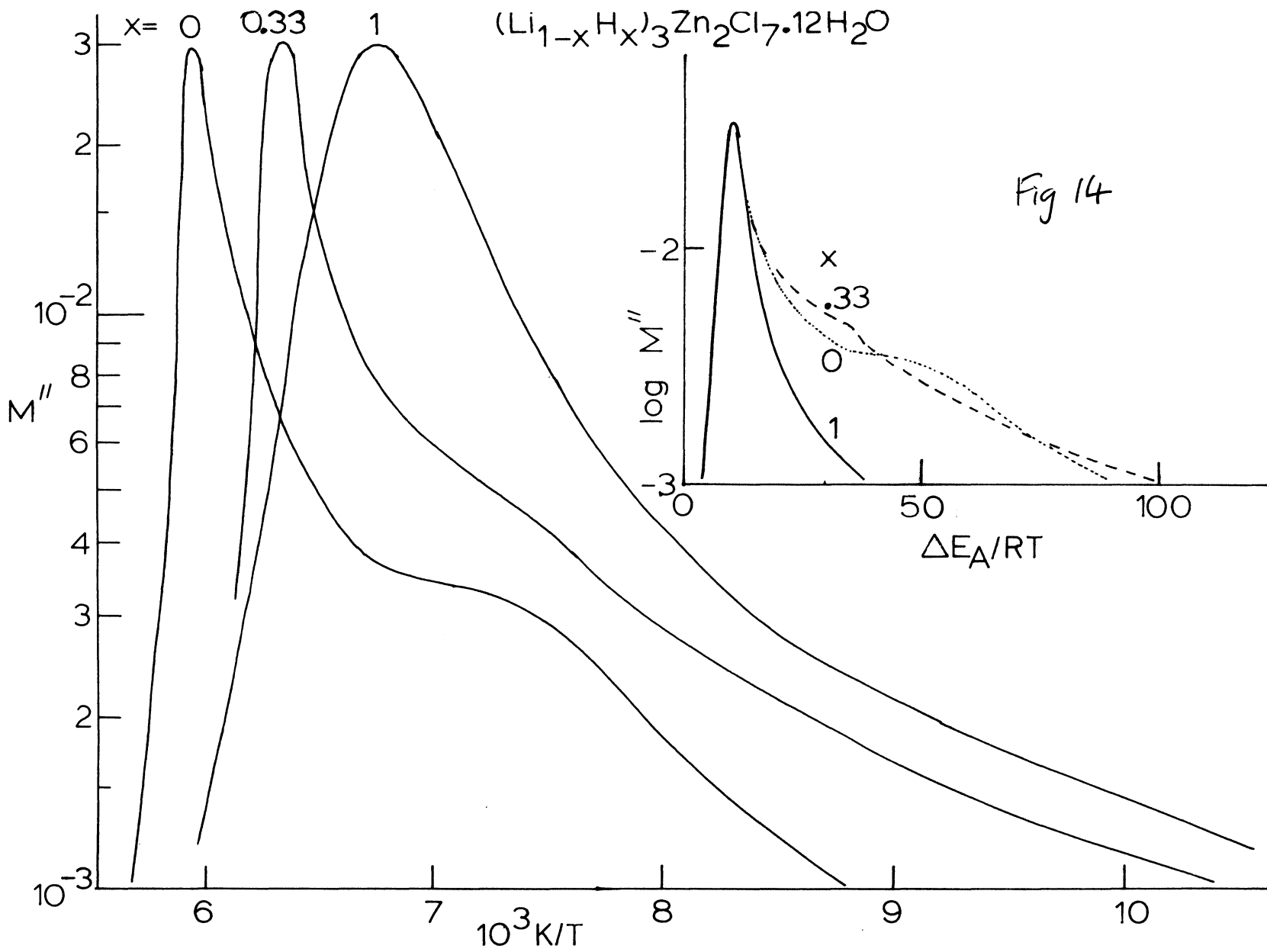


Fig 12

Fig 13





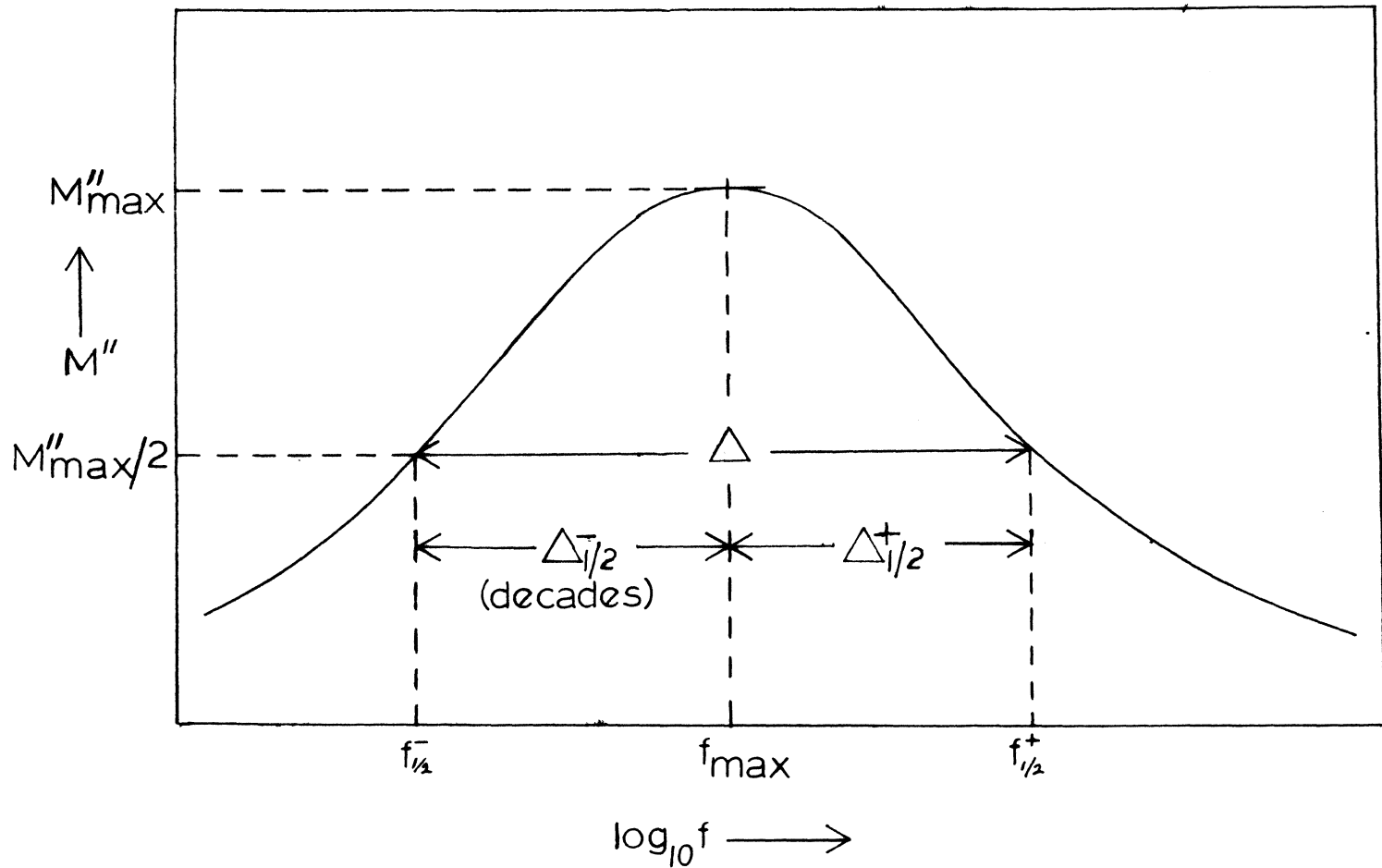


Fig A2-1

Fig A2-2

